



Quantitative 3D orientation analysis of particles and voids to differentiate hand-built pottery forming techniques using X-ray microtomography and neutron tomography

John Gait^{1,2} · Katalin Bajnok^{1,3} · Veronika Szilágyi⁴ · Imre Szent⁵ · Ákos Kukovecz⁵ · Zoltán Kis⁴

Received: 19 May 2022 / Accepted: 31 October 2022 / Published online: 17 November 2022
© The Author(s) 2022

Abstract

This article describes the quantitative analysis of the 3D orientation of objects (i.e. particles and voids) within pottery fabrics to differentiate two categories of pottery hand-building primary forming techniques, specifically percussion-building and coil-building, comparing the use of two independent non-destructive imaging modalities, X-ray microtomography (μ -CT) and neutron tomography (NT). For this purpose, series of experimental organic-tempered vessels and coil sections were analysed. For both imaging modalities, two separate systems were employed for quantitatively describing both the orientation of individual objects, as well as the collective preferential alignment of objects within samples, utilising respectively polar and azimuth angles within a spherical coordinate system, and projected sizes within a positive Cartesian coordinate system. While the former provided full descriptions of the orientations of objects within 3D space, the latter, through a ratio dubbed here the ‘Orientation Index’ (OI), gave a simple numerical value with which the investigated samples were differentiated according to forming technique. Both imaging modalities were able to differentiate between coil-built and percussion-built vessels with a high degree of confidence, with the strength of these findings additionally demonstrated through extensive statistical modelling using Monte Carlo simulations. Despite differences in resolution and differences in the attenuation of X-rays and neutrons, μ -CT and NT were shown to provide comparable results. The findings presented here broadly agree with earlier studies; however, the quantitative and three-dimensional nature of the results enables more subtle features to be identified, while additionally, in principle, the non-destructive nature of both imaging techniques facilitates such structural analysis without recourse to invasive sampling.

Keywords Pottery forming techniques · 3D imaging · Quantitative orientation analysis · X-ray microtomography · Neutron tomography · Monte Carlo simulations

Introduction

The understanding of pottery production techniques has long been a central area of interest within archaeology, both from the perspective of the history of technology, but also with regard to identifying culturally specific modes of material culture production and determining the social and historical mechanisms underlying the transmission of technological knowledge and practices. Pottery production is commonly conceptualised by archaeologists and anthropologists as a sequence of discrete stages (e.g. Rye 1981), with the choices and actions made at each stage influenced by not only material, physical, or technical necessities, but also by a range of social, economic, and cultural factors of which the potter may, or may not, be directly aware. From this approach, certain stages, such

✉ John Gait
john.gait@ek-cer.hu

¹ Neutron Spectroscopy Department, Centre for Energy Research, ELKH, Budapest, Hungary

² Department of Scientific Research, The British Museum, London, UK

³ Institute of Archaeological Sciences, Eötvös Loránd University, Budapest, Hungary

⁴ Nuclear Analysis and Radiography Department, Centre for Energy Research, ELKH, Budapest, Hungary

⁵ Department of Applied and Environmental Chemistry, Interdisciplinary Excellence Centre, University of Szeged, Szeged, Hungary

as the selection and preparation of raw materials or primary forming, are typically regarded as being conservative or habitual, reflecting historically embedded values or traditions, often passed between successive generations through socially governed networks of learning (e.g. Gosselain 2000, 2008). Other stages of production, such as decoration, are seen as potentially reflecting more transient fashions or superficial social interactions (e.g. Gosselain 2000). The investigation of primary forming techniques, therefore, may offer some insights into long-lived social practices, and as such may present a different perspective to that offered by purely typological classifications of pottery morphology or decoration.

A wide range of analytical techniques have been applied within archaeological pottery studies to investigate primary forming techniques, focusing either on surface features or on internal structures (Thér 2020). While surface features are comparatively easy to record and assess, typically without the need for invasive sampling, they are prone to being hidden or destroyed by subsequent stages of production (e.g. secondary forming, surface modification, decoration), use, burial conditions, or removed by excessive cleaning following archaeological recovery. By contrast, while techniques that examine the structure of pottery fabrics may be unaffected by such specific difficulties, they have conventionally required invasive or destructive sampling (e.g. fresh breaks or thin sections), or may rely on detecting features that are not always present (e.g. coil joins). For both approaches, however, analysis has often relied on the qualitative visual assessment of subtle parameters, leading to subjective interpretations of forming techniques, which in turn inhibit the integration of results from different research teams. In light of such criticisms, therefore, there is an apparent need for non-destructive techniques capable of examining the internal structure of pottery fabrics in a more objective manner, in order to facilitate better comparisons both between samples and investigators.

With regard to the identification of forming techniques through examination of pottery fabric structures, recent developments have progressed independently along two lines, namely in the application of X-ray computed tomography (CT) and X-ray microtomography (μ -CT), and the quantitative analysis of the preferential orientation of particles and voids (collectively termed here 'objects'). In the present study, we demonstrate how these two approaches may be combined to provide a powerful, non-invasive, and non-destructive method for the identification of primary forming techniques. In order to show the strength and versatility of such an approach, we separately demonstrate how the analysis of object orientations can also be undertaken using another form of tomographic imaging, neutron tomography (NT).

X-ray and neutron imaging

CT and μ -CT imaging techniques may be used to investigate the internal structure of various types of artefacts and materials, including ceramics, by displaying spatially resolved differences in the attenuation of incident X-ray beams (e.g. Buzug 2008). As X-rays generally display greater attenuation with increasing atomic number, the structure revealed largely corresponds to differences in material density. Consequently, with regard to pottery, voids may be most readily differentiated from the surrounding ceramic matrix due to their low X-ray attenuation. Similarly, certain types of aplastic inclusions displaying higher X-ray attenuation than the matrices may also be differentiated, although generally not as clearly as voids (e.g. Berg 2008; Kahl and Ramminger 2012; Thér 2020, p. 12), while crushed ceramic 'grog' temper may be especially difficult to detect when its attenuation is close to that of the host matrix. The exploitation of the differential attenuation of X-rays by various materials applies equally whether objects are examined by conventional 2D radiography or by 3D tomography. However, the greater clarity of imaging afforded by the latter arises from its ability to isolate spatially resolved differences in attenuation within a discrete plane, as opposed to presenting the cumulative attenuation throughout the entire thickness of a sample, where multiple voids or particles may appear to overlap.

Neutron imaging and neutron tomography (Bilheux et al. 2009) work in a similar manner to X-ray imaging techniques, but rely instead on the differential attenuation of an incident beam of neutrons and therefore may present a potentially different, often complementary, view of the internal structure of artefacts and materials. The lack of electrical charge enables neutrons to penetrate to large depths (typically several cm for the lower energy cold and thermal neutrons), and attenuation depends on the probability of interaction between the incident neutrons and the atomic nuclei of the target sample. Consequently, neutron attenuation is strongly influenced by the structure of the target nuclei and may vary considerably between different isotopes of the same element (e.g. Lehmann and Kaestner 2009). Unlike X-rays, neutrons may show high attenuation even for light elements such as hydrogen (especially ^1H), and therefore may be more sensitive for the imaging of organic materials. This higher sensitivity might, theoretically, provide an advantage in the imaging of organic inclusions or temper within pottery. However, as carbon shows comparatively low neutron attenuation, it may be called into question whether the carbonised remnants of organic inclusions present within pottery after firing are more visible in NT than voids or other types of inclusions.

CT and NT have been shown to be especially suited to the examination of cultural heritage artefacts as, in principle, the techniques are non-invasive and non-destructive. In practice, however, owing to instrumental spatial limitations as well as to improve image resolution, prior destructive sampling or, as in the case of pottery, the use of previously broken fragments, may be required. Thus far, NT has been applied to a wide variety of materials (e.g. Lehmann 2018; Mannes and Lehmann 2022), particularly metals, and although it has been used to image pottery vessels (Abraham et al. 2014; Szilágyi et al. 2016), it has not been applied to the examination of pottery forming techniques specifically. CT and μ -CT have seen greater application generally, and with regard to the study of pottery forming techniques have been most commonly used to identify macroscopic structural features such as the joins between coils or slabs (e.g. Bernardini et al. 2019; Kahl and Ramminger 2012; Kozatsas et al. 2018; Takenouchi and Yamahana 2021), or, in a qualitative manner, to examine the orientation of particles and voids (Kahl and Ramminger 2012; Neumannová et al. 2017; Park et al. 2019; Sanger et al. 2013; Sanger 2016). In this capacity, the reconstructed 3D models of CT and μ -CT data have been used as means by which to produce 2D 'slices' of the macro- and mesoscopic structural features of the fabric of vessels or sherds in specific desired orientations, which are then assessed by eye for diagnostic features in much the same manner as has previously been undertaken for images produced using flat-bed radiography (e.g. Berg 2008; Carr 1990; Rye 1977) or thin sections (e.g. Whitbread 1996; Woods 1985).

A limiting factor for any radiographic or tomographic imaging system is the spatial resolution, which in the case of CT and μ -CT ranges from 10^{-2} – 10^2 μm , while for NT resolutions of 10^1 – 10^3 μm are typical (Szilágyi et al. 2016). While the resolutions of NT and CT systems are notably poorer than that obtainable by μ -CT, they nonetheless encompass the size range of inclusions and voids commonly described within pottery fabrics using optical imaging techniques; as such, tomographic imaging techniques would appear capable of offering structural information with a level of detail comparable to that offered through thin section petrography or the examination of fresh breaks with a stereomicroscope, but with the additional advantage of non-destructive 3D imaging.

Despite their potential advantages, tomographic imaging techniques nonetheless share many of the same potential difficulties encountered with other techniques (e.g. ceramic petrography) with regard to the identification of pottery primary forming techniques. In the first instance, the visibility of macro-structural features, such as joins, is largely dependent on the presence of sizeable voids within fabrics, resulting from the incomplete merging of constituent elements (i.e. coils or slabs) during forming processes. As

these voids represent areas of structural weakness, it may be expected that in most instances potters sought to minimise their occurrence by intentionally merging elements together; consequently, when identified, these features may reflect the exceptions rather than the norms of production. The size of the constituent forming elements relative to the size of the sherds or vessels analysed may also influence the frequency with which joins may be detected. This may result in joins not being detected at all, especially in sherds that are smaller than the initial forming elements. To counter this difficulty, it may be necessary to analyse comparatively large sherds, which in turn may encounter instrumental spatial limitations and/or increase the required processing time. Furthermore, as joins represent areas of structural weakness, there is an increased tendency for pottery to preferentially break along these features, thereby reducing the chances of detecting joins within pottery sherds. Such difficulties entail that, in practice, the detection of diagnostic macro-structural features may be highly variable both within individual vessels as well as between the products of different potters.

The nature of the forming techniques themselves influences the extent to which they may be positively identified by characteristic macro-structural elements. In this regard, while, for example, coil-building may be demonstrated in a tangential view by the presence of joins aligned to the vessel rim, or slab-building by irregularly orientated joins (e.g. Rye 1981; Vandiver 1987), other techniques, such as drawing, pinching, simple moulding, or the percussive 'tamper-and-concave-anvil' technique (Sterner and David 2003), do not display comparable characteristic macro-structural features. However, given the variability in the extent to which joins may be preserved or detected in coil- or slab-building, their absence in imaging data cannot necessarily be interpreted as positive evidence for the use of, for example, percussive techniques.

Other potential criticisms of tomographic imaging arise from the way in which the data have often been evaluated and interpreted. In many instances extracted 2D images are examined in a qualitative, visual manner, which, as with similar analyses of thin sections or fresh fracture surfaces, may lead to subjective interpretations of forming techniques, thereby inhibiting the integration of results from different research teams. Furthermore, as examined further below, 2D images are limited with regard to the information that they are able to convey, and the extraction of isolated 2D slices as a precursor to analysis would appear to undermine one of the principal advantages of tomographic imaging, namely to provide three-dimensional structural information.

A promising method of using 3D information from μ -CT imaging is presented in a recent paper (Coli et al. 2022), which introduces a classical image processing tool (the Hough transform) for the detection of expected geometrical patterns in the porous structure of ceramic sherds. This

approach was shown to be able to differentiate between coil-building and the recently proposed, unusual ‘Spiralled Patchwork Technology’ technique (Gomart et al. 2017) using quantitative metrics, and accordingly represents an important step forward. However, more generally, the application of this approach may be limited by its need for prior assumptions regarding the forming techniques expected.

Preferential alignment of objects (particles and/or voids)

The preferential orientation of objects within ceramic fabrics has also been advocated as a means to determine the primary forming techniques of pottery, with assessments made using a variety of techniques including ceramic thin sections (e.g. Courty and Roux 1995; Reedy et al. 2014a, b; Roux and Courty 1998; Thér, 2016; Thér et al. 2019; Thér and Mangel 2021; Thér and Toms 2016; Whitbread 1996; Woods 1985), thick sections (e.g. Lindahl and Pikirayi 2010; Ross et al. 2018), 2D X-ray radiographs (e.g. Berg 2008, 2009; Carr 1990; Choleva et al. 2020; Greene et al. 2017; Livingstone Smith & Viseyrias 2010; Pierret et al. 1996; Pierret and Moran 1996; Rye 1977, 1981; Türkteki 2014), or visual inspections of cross-sectional fractures (e.g. Gait 2011; Quinn 2022, figs. 6.47, 6.51, 6.57). According to this approach, particles and voids in an unfired, plastic clay mass may become orientated in characteristic patterns as a result of the application of forces during primary forming. Subsequent stages of forming, usually performed after a period of drying, have been thought generally not to change the initial orientation of objects produced during primary forming; the principal exception to this being the paddle-and-anvil thinning technique that results in an additional alignment of objects towards vessel walls (Berg 2008, 2009; Rye 1981). However, more recently it has been suggested that, to the contrary, secondary forming techniques do in fact substantially alter the orientation of particles near the margins of the vessel walls (Thér 2016; Thér et al. 2019).

In practice, as noted by Thér et al. (2019, p. 2), the direction and extent of preferential orientation among observed objects have conventionally been assessed in purely qualitative manners, or by reference to ordinal scales, with comparatively few attempts to apply more quantitative approaches. More recently, improvements in digital image analysis have led to renewed interest in the quantitative evaluation of object orientations using photomicrographs of thin sections and more objective assessments of forming techniques (Thér 2016; Thér and Toms 2016).

Thin sections, thick sections, or fresh breaks, usually made horizontally, vertically, or tangentially to the structure of a vessel (Whitbread 1996, fig. 3), may be used to view the orientation of objects within 2D planes, with comparisons made between samples and/or against theoretical models of

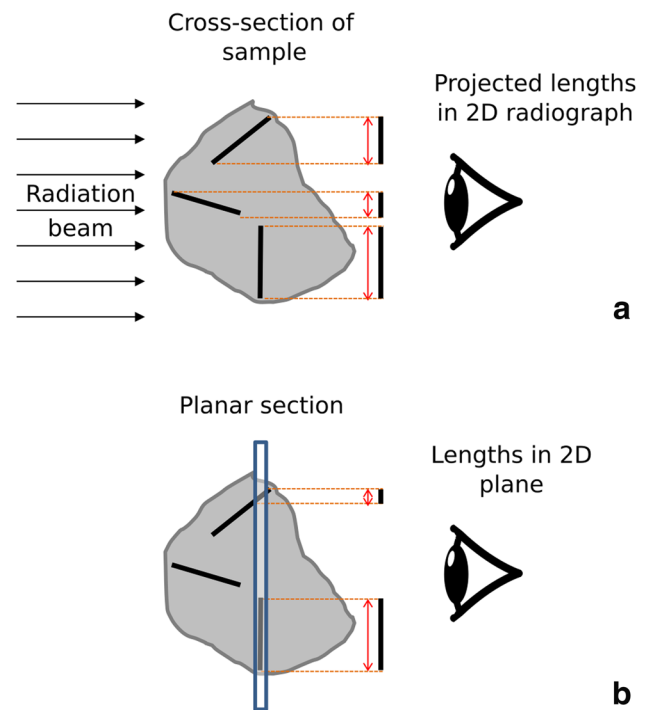


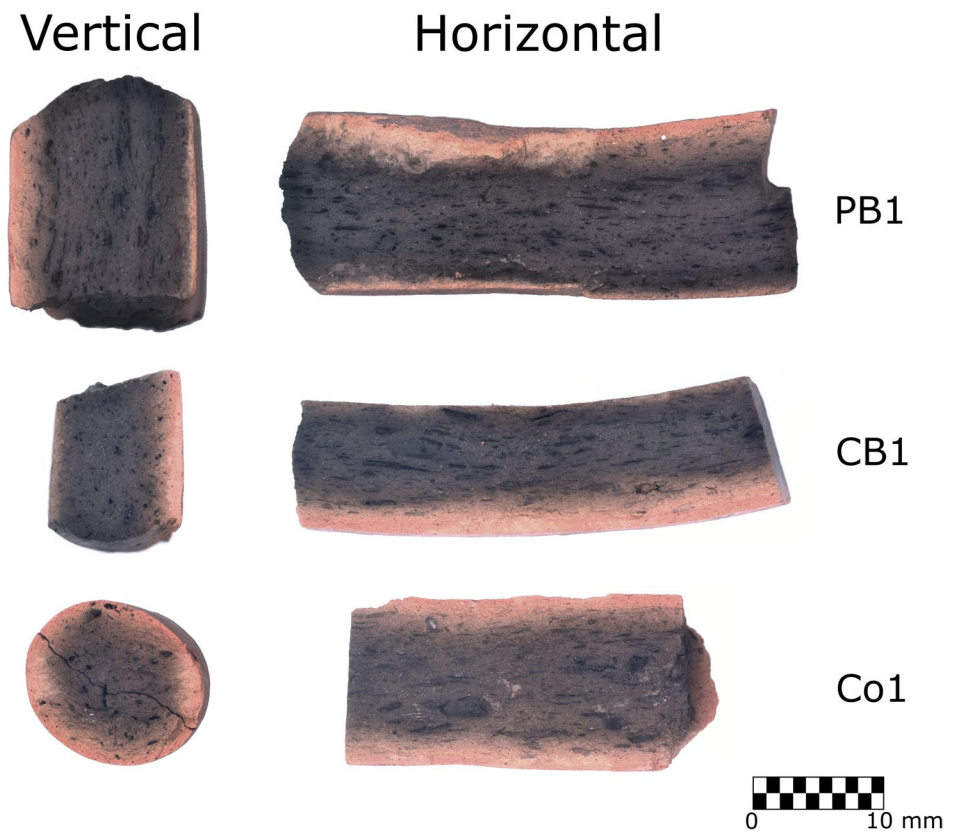
Fig. 1 Schematic diagrams showing potential differences in the apparent lengths of objects when viewed in 2D: **a** the foreshortening effect on three objects of equal length, and the differences in their projected lengths when seen in a 2D radiograph, resulting from their different orientations relative to the incident radiation beam; **b** lengths of objects seen in a 2D section (e.g. petrographic thin section, tomographic slice, or fresh fracture surface), resulting from the position and orientation of objects relative to the plane of the section



Fig. 2 Examples of a percussion-built (PB) and a coil-built (CB) experimental vessel, and a coil section (Co) analysed in this study

expected object orientations (e.g. Berg 2008; fig. 1; Carr 1990; fig. 1; Middleton 2005, fig. 4.8; Rye 1977, 1981; Thér 2020, fig. 9; Whitbread 1996, figs. 2, 3). In the approach developed by Thér (2016), the direction and extent of

Fig. 3 Vertical and horizontal cross-sectional fresh fracture surfaces of PB1, CB1, and Co1 after initial firing



preferential orientation within tangential and vertical thin sections were described by the mean and the circular standard deviation of the angles of objects. The use of thin sections necessarily entails destructive sampling, and tangential sections in particular may require larger samples and be more difficult to produce than conventional vertical sections. Furthermore, the necessity of identifying sufficient numbers of suitable objects in order to produce statistically significant results may require the use of large samples and/or limit the technique to fabrics with a high proportion of visible objects.

A more significant limitation of the use of thin sections, as with extracted 2D tomographic slices used in isolation, is the inability to simultaneously describe the orientation of objects or features within three dimensions. Indeed, in this regard, both approaches appear rather to conceptualise the features of interest (whether particles or voids, or macro-structural joins) as purely two-dimensional entities within isolated, and standardised, 2D orthogonal planes; in the case of the analysis of object orientations using two orthogonally orientated (e.g. tangential and vertical) thin sections, the data are commonly analysed independently of each other even though they originate from the same samples and therefore necessarily reflect the same underlying fabric structures.

A failure to conceptualise and evaluate objects as 3D entities may give rise to certain difficulties when attempting to

describe their size and shape, and hence to identify preferential orientation and to differentiate forming techniques. When viewed in different planes, anisometrically shaped 3D objects may appear as different 2D shapes with different resulting dimensions and angles of orientation. Such differences are most apparent with regard to acicular-shaped objects (such as fibres, where length greatly exceeds width and thickness) but also among elongated platy objects (such as grasses, where width is greater than thickness, but less than length) which may present a large longitudinal area but comparatively small transverse cross-sectional area; while such objects may be readily identified and counted in one plane, they may be missed (despite actually being present) and undercounted within another. As such, therefore, there are potential orientation-dependent biases in the quantification of objects, in the determination of spatial dimensions, and in the measurement of angles of orientation, which are further exaggerated when objects display preferential alignment in more than one axis. Not only may this make accurately describing individual objects more problematic, but potential biases in the ability to recognise and count the number of objects in each 2D view (due to relative differences in the areas each object presents) may adversely affect determination of the extent to which the objects collectively may be preferentially aligned. Such theoretical difficulties apply whether 2D planar views are assessed by eye

or through digital image analysis where smaller objects are necessarily ignored or filtered out, and/or where only the most elongated objects are counted. However, in practice, as nearly all pottery forming techniques result in objects having a preferred low angle of inclination to the surfaces of vessels, such potential difficulties may be minimised in tangential views, whereas they remain potentially significant in 2D vertical or horizontal views.

A related difficulty is the issue of foreshortening, which creates uncertainties in the simultaneous determination of the length and orientation of objects when examined in 2D. Accordingly, in the absence of any internal structural clues, it may be impossible to differentiate between the projected and real lengths of objects; for example, a short object orientated parallel to the plane of observation may appear identical to a long object inclined at an angle to the plane. This effect is particularly pronounced with radiographic images, and highlights the important, but often overlooked, difference between planar images (e.g. thin sections, fracture surfaces, or tomographic slices) and radiographs with regard to the interpretation of object orientations (Fig. 1). While X-ray (and neutron) radiographs are 2D images, they nonetheless represent the *cumulative* attenuation of a beam through the entire thickness of a sample in a specified direction, thereby resulting in potentially large variations in the projected length of an object depending on its orientation. By contrast, within planar sections, this foreshortening effect does not occur (or in the case of thin sections is minimal), although there may still be large differences between the length of an object seen in a planar section and its original length in a sample.

Research objectives and strategy

In this article, we aim to demonstrate the application of two independent, non-invasive, and non-destructive tomographic imaging techniques, which combined with digital image analysis and quantitative evaluation of structural features of pottery fabrics may be used to identify primary forming techniques. More specifically, we utilise the ability of μ -CT and NT to provide three-dimensional spatially resolved information on the shape, orientation, and frequency of particles and voids within fabrics, and the quantifiable differences in these parameters to differentiate between coil-built and percussion-built vessels.

Choice of forming techniques

To demonstrate the specific application of 3D object orientation analysis, we undertake the differentiation of two common categories of primary forming techniques, coil-building (CB) and percussion-building (PB), using experimental

vessels made under known conditions. While it is envisaged that the analytical techniques employed may also be able to differentiate other forming techniques, these two categories of hand-building techniques are selected so as to broaden the range of information available within a field that has hitherto previously largely focused on the identification of coil-building and various wheel-based techniques (e.g. Berg 2008; Courty and Roux 1995; Roux and Courty 1998; Thér and Toms 2016). The differentiation of hand-building techniques is also of particular relevance in many archaeological contexts where wheel-based techniques are known not to have been practiced. In this regard, the present choice of forming techniques to investigate is informed by one of the authors' research interests in the cultural dynamics of Neolithic and Early Bronze Age Lower Nubia (Gait 2011), where the use of coil-building and a form of the 'tamper-and-concave-anvil' (TCA) technique of percussion-building have both been suggested (Nordström 1972; Williams 1983).

Coil- and percussion-building techniques are also known from previous studies to be difficult to differentiate through 2D object orientation analysis. While a recent experimental study that included coil- and slab-building (which displays many similarities in fabric structure to percussion-building techniques (Rye 1981)) found distinct patterns of orientation in preformed constituent elements (i.e. coil sections and slabs), it could not consistently differentiate all vessels made with these techniques, and concluded that in some instances the additional forces used to join elements resulted in a significant reorientation of objects and an overlap in the distributions of the examined samples (Thér et al. 2019). Consequently, the present study aims to investigate whether 3D object orientation analysis may offer an alternative approach to the differentiation of similar techniques.

Choice of materials

In order to detect the effects that forming techniques may have on the structure of pottery fabrics, it is necessary to utilise a tempering material that readily displays responses to these forming techniques, and that is of a material and size range that may be detected in both CT and NT. For these purposes, dried cattle dung may represent a suitable temper as, consisting primarily of fragments of partially digested grass of simultaneously elongated and flattened shape, there are large differences in the dimensions of each axis of the individual particles (i.e. typically, before firing, there is approximately an order of magnitude of difference between the length and width, and between the width and thickness, of each particle). Such differences in shape may facilitate the detection of object orientation, and similar organic materials have previously been used in other experimental pottery studies (Berg 2008; Foster 1989; Thér et al. 2019).

Furthermore, as demonstrated by previous radiographic studies, organic tempers, or the relic voids left after firing, are known to be readily identifiable within ceramic fabrics when examined by X-rays; with regard to NT, the use of organic tempers is also likely to be detected either as a result of the high neutron attenuation resulting from the presence of ^1H in any residual unfired particles, or, more probably, due to the low neutron attenuation of voids and carbon among entirely, or partially, combusted particles (from which ^1H has been lost). The size range of particles of dried cattle dung also typically exceeds the minimum sizes of features than can be detected by conventional μ -CT and NT systems.

The use of fibrous organic materials (including dried dung, chaff, moss, and other materials) as temper is also relevant from an archaeological perspective, being attested within the potting traditions of numerous cultures in various locations and chronological periods (e.g. Hamerow et al. 1994; London 1981; Nordström 1972; Sanger 2016; Tomber et al. 2011, and references therein).

Choice of imaging techniques

The use of two independent imaging techniques enables a degree of cross-verification of the results from each technique, but also permits some investigation into the various factors that might affect the analysis of object orientations in pottery fabrics. While μ -CT offers considerably better spatial resolution than either conventional CT or NT systems, such advantages in imaging need not necessarily confer benefits in the determination of object orientations and pottery forming techniques. Indeed, compared to larger CT or NT facilities, often capable of analysing large samples, or multiple samples simultaneously, the small size of the sample chamber of some μ -CT systems may be a greater disadvantage overall, potentially preventing the analysis of complete vessels or requiring the selection of smaller sherds. Consequently, by comparing the results from μ -CT and NT, this study also aims to determine whether there are significant analytical differences in the ability of high- and low-resolution imaging systems to differentiate forming techniques.

Although NT has previously been used in some cultural heritage applications, it has not been applied to the analysis of pottery forming techniques. The present study therefore represents an opportunity to potentially extend the analytical utility of NT. In addition, through the use of organic temper in the experimental vessels, this study will investigate whether the higher sensitivity of NT to organic materials, compared to X-ray-based techniques, may provide any advantages in the detection of particles in fired ceramics.

Methodology

Materials

A total of nine samples (PB1-3, CB1-3, Co1-3), from three series of fired pottery, were imaged by both μ -CT and NT. Both imaging techniques were performed using the same set of samples cut from each series, thereby eliminating potential discrepancies arising from differences within each vessel/coil section. Two of the series each consisted of three vessels made by an experienced potter using either a percussion-building (PB) or coil-building (CB) technique; the third series consisted of three sections of rolled coils (Co) selected from among those prepared as part of the coil-building process (Fig. 2). Prior to forming, clay pastes were prepared using a single, fine-grained commercial potting clay mixed with dried cattle dung as temper.

Coil-built vessels, and coil sections, were made in the manner commonly described in the archaeological literature (e.g. Rice 2007; Roux 2019; Rye 1981). Accordingly, for each vessel, a mass of prepared clay was rotated in a reciprocating manner on a flat surface while simultaneously being compressed, resulting in the lateral displacement of clay and the formation of long cylinders, or 'coils', of c. 1.2–1.3 cm diameter. Lengths of these coils were then laid one above the other, in circles of increasing diameter, with the successive layers joined together by downward compression and the merging of the outer edges of the coils. Layering continued in this fashion until the desired height of the vessel was reached, usually equivalent to c. 7–10 coil layers. The interior and exterior surfaces of the vessels were then lightly smoothed in order to produce a more even surface but without substantially altering the shape of the vessel.

Percussion-built vessels were made following a variant of the TCA technique (e.g. Gosselain 2008; Sterner and David 2003). Prior to commencing the shaping of the vessels, a shallow, rounded depression was excavated from a ground surface, and a small, slightly tapered, round-based 'tamper' or 'hammer' was formed from clay; both the depression and tamper were allowed to dry and harden naturally before use. For each vessel, a single mass of tempered clay was placed within the depression and repeatedly struck with the tamper, resulting in the lateral displacement of the clay. The position of the clay mass within the depression was periodically adjusted as the wall of the vessel was formed, until the desired size and shape of the vessel were achieved. Finally, the rim of the vessel was trimmed and smoothed.

Each vessel took the form of a simple open bowl. Across the entire assemblage, the six vessels ranged from

8.5 to 12 cm in height, from 28 to 32.5 cm in rim diameter, and from 1.1 to 1.6 cm in wall thickness. This simple vessel shape was chosen in order to minimise the need for additional forming techniques (e.g. pushing, or pinching) that might be required for more complex shapes. The slight variations in size and shape among the vessels were considered not to adversely influence the subsequent analyses and comparisons.

The vessels and coil sections were fired together in an electric kiln at 650 °C, resulting in the oxidation of the walls and margins to a light red-brown colour, with voids corresponding to burn-out dung particles; the cores were commonly dark grey to black in colour with frequent partially combusted, carbonised particles of dung temper visible (Fig. 3). As such, the firing achieved variations in colour and composition also frequently seen in archaeological specimens of organic tempered pottery.

Samples measuring c. 5 by 6 cm were cut from the upper section of each fired vessel, retaining a portion of the rim in order to provide a reference line by which the tomograms were subsequently orientated. The samples of coil sections, c. 1.2–1.3 cm diameter, were cut to lengths of c. 4.5 cm. All the samples were imaged by μ -CT and NT. After tomographic imaging, vertical and horizontal thin sections were prepared from the fired samples, using dyed resin to enhance the visibility of the voids. Two samples (CB1 and PB1) were then refired at 700 °C, with a soaking time of 2 h, in order to achieve the complete combustion of the dung temper. Following refiring, the walls and entire cross-section of each sample were a near-uniform light red-brown colour, with frequent voids visible. The refired samples were then imaged by NT for a second time.

Imaging with X-rays and neutrons

In computed tomography imaging multiple, differently orientated, 2D projectional radiographs may be used to create a virtual reality 3D digital model of the surfaces and internal structure of a sample (Banhart 2008; Bilheux et al. 2009). The constituent radiographs themselves are projected shadow images representing the interaction between an incident beam of penetrating radiation (e.g. X-rays or neutrons) and the materials of a sample placed in the path of the beam. In practice, the different projection angles are achieved by incrementally rotating a sample on a motorised turntable situated between the radiation source (an X-ray tube or a beam port at a nuclear reactor generating neutrons) and the instrument detector (flat panel for X-rays, scintillator screen for neutrons). The resulting radiographs from each sample are then collectively mathematically reconstructed (e.g. using a filtered back-projection algorithm) into a sequential stack of Fourier slices orientated perpendicular to the plane of

the projected radiographs. Each stack of slices is then rendered into a single 3D model in which component features representing contiguous volumes of specified ranges of attenuation (or ‘greyscale values’) may be isolated (i.e. segmented) and then measured. The 3D model may also be visually reorientated by the user and recut in planes of any desired orientation to provide tomographic slices (or ‘tomograms’). Importantly, whereas projectional radiographs display the spatial cumulative attenuation through the entire thickness of a sample in each rotational position, the tomographic slices can be thought of as thin layers through a target sample, each mapping the spatial distribution of the materials’ attenuation coefficients in that plane. As with radiographs, the type and size of features that may be displayed in reconstructed 3D models depend on the thickness and composition of the samples being measured, the energy distribution of the radiation, and various specific instrumental parameters (e.g. the spatial resolution of the detector, the distance between the sample and the detector plane, and the optical system of the instrument).

One of the most important characteristics of an imaging system is its spatial resolution, which mostly determines the smallest size of a detectable feature. It plays a significant role in our evaluations; therefore, further details are given here. The theoretically attainable optimal resolution (calculated using the Nyquist sampling theorem) is twice the so-called effective pixel size. The effective pixel size for X-ray-based imaging systems is the native pixel size of the flat panel detector divided by the magnification of the beam; whereas for neutron imaging systems operating with near parallel neutron beams, the optimal resolution is determined by the size of the area on the scintillator screen seen by one native camera pixel. In most imaging systems, the best spatial resolutions are significantly better for X-rays than for neutrons.

In the present study, a total of nine samples (PB1-3, CB1-3, Co1-3) were imaged using two different methods, μ -CT and NT; in addition, two samples (CB1 and PB1) were imaged again by NT after refiring. For X-ray tomography, the Bruker SkyScan2211 X-ray system of the University of Szeged was operated in μ -CT mode with a flat panel detector with an effective pixel size of 40.00 μ m (camera pixel size = 74.8 μ m, sample to camera distance = 132 mm, source to camera distance = 284 mm, magnification = 1.87). This gave a theoretical optimal spatial resolution of 80 μ m for 2D projections, deteriorating to c. 90–100 μ m for 3D images. The X-ray source operated at 110 kV (Co1, Co2, Co3) and at 120 kV (CB1, CB2, PB1) with a 0.5 mm Ti filter, and at 135 kV (CB3, PB2, PB3) with 0.5 mm Cu filter. The exposure time was 50 ms for each of the 1801 projected images obtained per sample. The μ -CT data were reconstructed using the beam-hardening, post alignment, and ring artefact

corrections implemented in the instrument's NRecon reconstruction software (Bruker 2005).

For neutron tomographic scans, the RAD neutron imaging station of the Budapest Neutron Centre (Kis et al. 2015) was operated with a 100- μm -thick LiF-based scintillator screen, with an effective pixel size of 43 μm , and an Andor Neo5.5 sCMOS camera with a 105-mm focal length lens. Owing to the large sample chamber, it was possible to image multiple samples simultaneously, with individual samples subsequently isolated during data processing. Samples PB1-3 and CB1-3 were imaged together with a sample-to-screen distance of 50 mm, while samples Co1-3, being slightly smaller, were placed closer to the detector with a sample-to-screen distance of 35 mm. For the PB and CB samples, the measured best spatial resolution was 280 μm in 2D images, deteriorating to c. 300 μm in 3D images, whereas for the Co samples slightly improved resolutions of 230 μm in 2D and c. 250 μm in 3D were obtained. These values are significantly poorer for NT than for $\mu\text{-CT}$ for two main reasons: (a) in the scintillation process, the neutron is converted into visible light through an alpha-particle reaction, where the emerging alpha-particle moves isotropically several tens of microns through the scintillator's matter before producing visible light; (b) the geometrical blurring of the beam resulting from the non-point-like structure of the neutron source. The thermal neutron flux was $4.2 \times 10^7 \text{ cm}^{-2} \text{ s}^{-1}$ with a L/D collimation ratio of 214. The exposure time was 25 s for each of the 1126 projected images per sample. The projected radiographs were preprocessed using FIJI (Schindelin et al. 2012), and reconstructed into Fourier slices using Octopus 8.9 (Vlassenbroeck et al. 2007). Fortunately, beam hardening effects were less pronounced in the neutron tomograms compared to the X-ray tomograms.

3D data treatment

For both $\mu\text{-CT}$ and NT, the Fourier slice stacks for each sample were rendered into 3D models and evaluated using VGStudio MAX 3.2 (Volume Graphics 2019) and ORS Dragonfly 2022.1 (Object Research Systems 2022) software packages. Each CT model was manually aligned to the software's main scene axes (x , y , and z) (Fig. 4) using the rim and exterior wall of each sample as references; the NT models were then mathematically registered to their corresponding CT models. For each model, particles/voids were segmented from the surrounding matrix using the VGDefX algorithm of the Enhanced Porosity/Inclusion analysis module in VGStudio. As, at this stage, the compositions of the particles or voids detected by the software were not known, the term 'object' was used to refer to any solid particle or void that was segmented from the matrix. Due mainly to better spatial resolution, the number of segmented objects detected by $\mu\text{-CT}$ far exceeded that detected by NT.

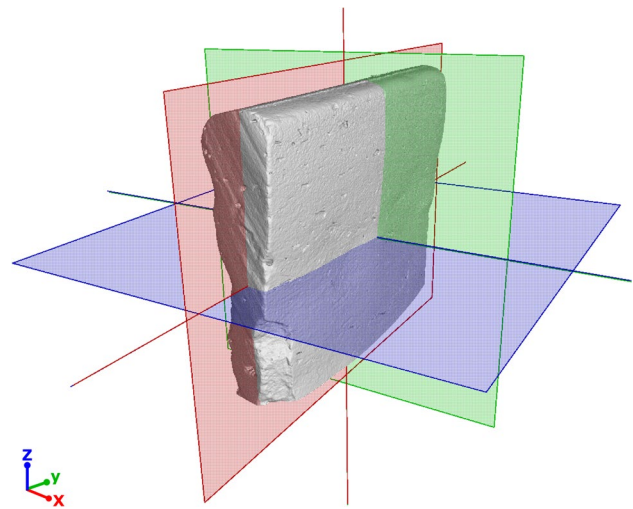


Fig. 4 Alignment of a vessel sample in the VGStudio 3D environment, showing the horizontal section (x - y plane, blue), vertical section (x - z plane, green), and tangential section (y - z plane, red). The x -axis represents the wall thickness of a sample measured perpendicular to the exterior surface; the y -axis represents the horizontal axis, parallel to a tangent to the rim of the sample; the z -axis represents the vertical axis, perpendicular to the rim of the sample and parallel to the walls of the sample

The datasets of segmented objects were subsequently analysed in Dragonfly, which calculated various parameters for each object including voxel count, volume, polar angle, azimuth angle, minimum and maximum Cartesian coordinates, and 3D aspect ratio (Object Research Systems 2022). No steps were taken to mitigate the minor systematic error resulting from the slight curvature of the sherds; this was because of both its limited extent and its approximately equal effect on each sample (the same difficulty is also encountered with tangential thin sections, which also do not compensate for such curvature).

The raw data generated in Dragonfly was then subsequently constrained by the use of object voxel and aspect ratio filters. Minimum voxel filters were guided by the highest spatial resolutions of the imaging systems (i.e. 156 and 398 voxels, equivalent to 0.01 mm^3 and 0.03 mm^3 , in $\mu\text{-CT}$ and NT respectively), while an arbitrary maximum volume was set at 30 mm^3 . While the difference between the real volume of a sphere and that calculated from the cumulative total of its constituent voxels may be significant for objects of less than c. 4400 voxels (Kaestner et al. 2017), similar discrepancies were not found to be very significant with regard to either the principal variables of interest in the present study (i.e. projected sizes and polar and azimuth angles) or the ultimate differentiation of forming techniques; therefore, it was possible to set the minimum voxel counts to comparatively low values, thereby retaining larger frequencies of objects. In addition, the datasets of segmented

objects were constrained by aspect ratio, between 0 and 0.3 for both imaging modalities, where an aspect ratio of 0 corresponds to a perfect rod of unit width and an aspect ratio of 1 corresponds to a sphere (Object Research Systems 2022). The maximum value of the aspect ratio was selected as a compromise between the preferential selection of more elongated objects better able to display the effects of forming techniques, and the need to retain sufficient numbers of objects to enable robust statistical results. The resulting filtered datasets were then used for the subsequent quantitative analyses.

For each 3D model, the segmented and filtered data were stored in CSV spreadsheets and then subsequently evaluated in Microsoft Excel. For each sample, in both μ -CT and NT, two descriptive systems were utilised. In the first instance, the relative orientation of each object was described by its projected sizes, calculated as the magnitude of the difference between the maximum and minimum values in each axis of a Cartesian coordinate system of Euclidian space, thereby transforming the object into the positive spatial octant (Fig. 5a). The maximum length of each object, L , was calculated as the space diagonal of the bounding box formed by the constituent axial projections.

Using the projected sizes, a measure of the relative extent of collective preferential alignment of objects within each sample was also calculated, termed here the ‘Orientation Index’ (OI).

The OI was defined as the absolute value of the difference between the relative sizes of the mean x -axis and z -axis projections, normalised with respect to the mean y -axis projection (which consistently displayed the largest mean values).

$$OI = \left| \frac{\left(\frac{1}{n} \left(\sum_{i=1}^n \text{proj}_{-x_i} \right) \right) - \left(\frac{1}{n} \left(\sum_{i=1}^n \text{proj}_{-z_i} \right) \right)}{\frac{1}{n} \left(\sum_{i=1}^n \text{proj}_{-y_i} \right)} \right|$$

A second descriptive system described each object with reference to three variables (θ , ϕ , L') within a spherical coordinate system (Fig. 5b; Fisher et al. 1993). The polar angle (θ), ranging from 0 to 90°, equalled the magnitude of the minimum angle subtended between the y -axis and the principal axis through each object (determined as the axis belonging to the shortest eigenvalue of the tensor of inertia of the object, considering the volume each object to be of uniform and equal density). The azimuth angle (ϕ), ranging from 0 to 360°, equalled the angle subtended between the positive x -axis and the projection of the principal axis of each object onto the x - z plane. As axial data, values of ϕ in the range 180–360° correspond to values of 0–180°, and by convention mean values are reported in this lower range. The length of the principal axis of each object within the spherical coordinate system, L' , was approximated by the maximum Feret length (measured in 3D space).

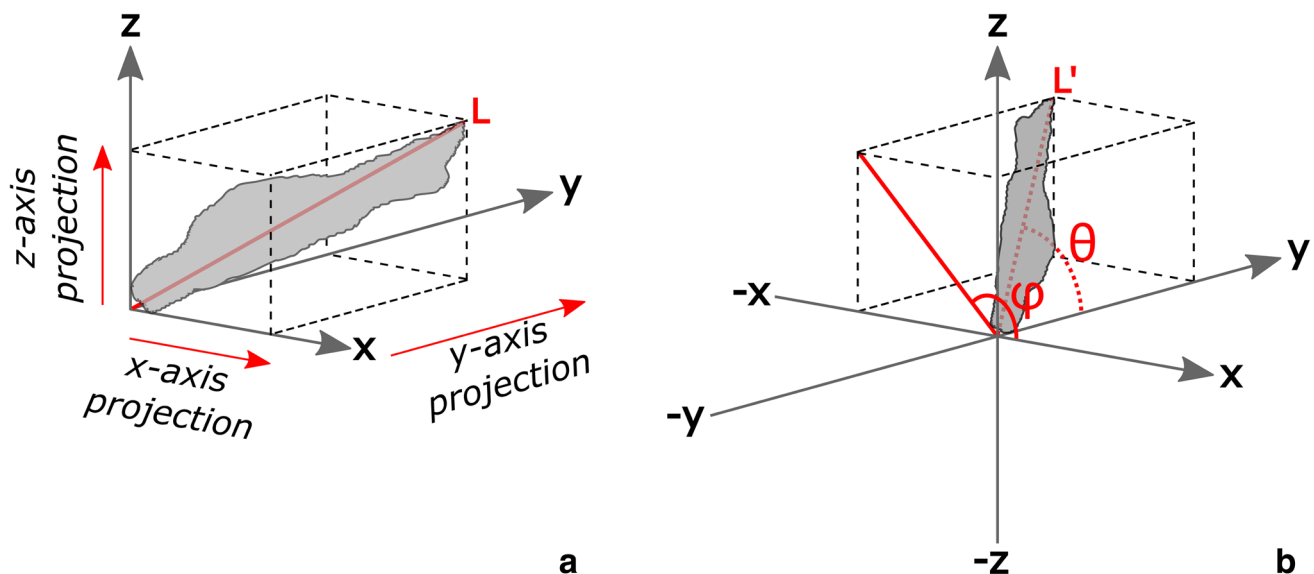


Fig. 5 Schematic diagrams of two systems for describing the orientation of an object in 3D space: **a** relative orientation of an object described by a bounding box formed by its projected sizes in each Cartesian axis, spatially transformed into the positive octant of the coordinate system; maximum length, L (solid red line), measured as the space diagonal of the bounding box; **b** orientation of an object described by polar angle, θ , azimuth angle, ϕ , and length, L' , in a spherical coordinate system. θ (0–90°, dotted red arc) measured as the magnitude of the minimum angle subtended between the y -axis

and the principal axis of each object (determined as the axis belonging to the shortest eigenvalue of the tensor of inertia of the object); ϕ (0–360°, solid red arc) measured as the angle subtended between the positive x -axis and the projection of the principal axis of each object onto the x - z plane (solid red line); L' (dotted red line), measured as the maximum Feret diameter of each object. The spherical coordinates retain the position and orientation of each object, whether in positive or negative areas of the spatial system

Within the spherical coordinate system, the polar angle represents only the magnitude of the angular deviation of objects from the y -axis, and as such, does not indicate the specific rotational position around the y -axis occupied by any specific object; this rotational position is instead expressed by the azimuth angle. Consequently, although the polar angle may superficially reassemble the angle of inclination of the long axis of an object above the horizon in a conventional 2D tangential thin section or radiograph, there are significant differences. Specifically, the polar angle corresponds to the maximum angle of inclination that could be seen in a 2D tangential projection or slice, for an object with an azimuth angle of 90° . For any other objects with the same polar angle, but with either higher or lower azimuth angle values, the projected angle of inclination seen in a 2D tangential plane would be less than the value of its polar angle.

Statistical analytical methods

The data from each sample were evaluated to determine whether primary forming techniques could be differentiated by the preferential orientation of objects, and if such determinations differed between μ -CT and NT imaging techniques. For these purposes, statistical analyses were performed using the built-in routines of Excel together with the XLStat (Addinsoft 2021) and Simulacion5 (Simulaci3n5 2022) add-ins.

Excel was used to calculate the arithmetic mean, standard deviation (SD), and standard error of the means (SE) for the lengths, projected sizes, and angles of the objects, with azimuth angles treated as axial circular data (Fisher 1995). Visualisations of circular data were made using Oriana 4.02 (Kovach Computing Services 2013). Comparisons of object length distributions of fired and refired sherds were made using the nonparametric Kolmogorov–Smirnov hypothesis test in XLStat.

A kind of sensitivity analysis, focusing on the robustness of the results (termed here “robustness analysis” (RA)), using Monte Carlo simulations was subsequently performed either on standard statistics (mean, SD, SE, etc.) or on the chosen variables (OI, θ , and ϕ) for each sample series (i.e. PB, CB, and Co) in each imaging modality using Simulacion5. RA was used to test the strength of the result by investigating the correlations between object volume and aspect ratio (termed here ‘parameters’) and the variables (OI, θ , and ϕ) To do this, a great many pairs of values were sampled from the distributions of the parameters, averaged across all three samples within each series of samples, to apply as either minimum (volume) or maximum (aspect ratio) filters in the RA process.

The stability of the variables against these parameters was determined using Simulacion5 applying Latin Hypercube sampling to 5000 simulations of each sample series in each

imaging modality. The necessary RA input data (volume and aspect ratio distributions, and the correlation between these parameters) were previously determined from the 3D datasets created by the VGStudio and Dragonfly software.

Qualitative description of 3D imaging

Structural features

The tomographic imaging, followed by segmentation of the rendered 3D models, resulted in the generation of large datasets of objects for each sample; typically consisting of up to several thousand objects for μ -CT and several hundred for NT, depending on the imaging parameters and filters applied. The large number of objects detected provided a detailed view of the internal structure of the samples (e.g. Fig. 6, see also Online Resource 1 for selected orthogonal tomographic slices of each sample), but, more significantly, also enabled robust statistical examination (see below). From a qualitative perspective, the 3D models of the PB and CB samples showed clear differences in the preferential orientations of objects. Accordingly, in the CB samples (Fig. 6b, e) objects tended to align more favourably towards the rim and walls of the samples and perpendicular to the direction of the thickness of the vessels (i.e. preferentially aligned in the direction of the y -axis of the imaging environment and perpendicular to the x - and z -axes). By contrast, among the PB samples (Fig. 6a, d), objects appeared to be preferentially aligned to the walls only (i.e. within a y - z plane, and perpendicular to the x -axis), and displayed no visually obvious preferential orientation in relation to the rims of the samples. Such patterns of orientation are in general agreement with those described in previous studies (e.g. Rye 1981).

Among the Co samples (Fig. 6c, f), the objects also displayed strong preferential orientation in the direction of the main axis of the coils (i.e. in the direction of the y -axis), similar to that seen in the CB samples. Consequently, from a qualitative perspective, it appears that much of the orientation seen in the CB samples was derived from the orientation already present in their constituent coil sections. However, the presentation of the preferential orientation of objects in the Co samples, when viewed in tomographic sections, differs in certain significant regards from previous presentations of similar phenomena. In the present study, partially combusted, elongated, fibrous particles of dung temper and/or corresponding relic voids appear as comparatively large elongated shapes in horizontal/tangential sections of the coil samples (Fig. 7a), and as small, equidimensional shapes in vertical sections (Fig. 7b). The horizontal/tangential planar view shown here is broadly comparable to that seen in Berg’s radiograph of a coil (Berg 2008, fig. 5). Nevertheless, there are pronounced differences in the appearance of the

Fig. 6 Rendered 3D models of selected samples, from μ -CT and NT, created using VGStudio. **a** PB1, μ -CT; **b** CB1, μ -CT; **c** Co1, μ -CT; **d** PB1, NT; **e** CB1, NT; **f** Co1, NT. Differences can be seen between the μ -CT and NT models in the number of objects detected; minimum volume of objects: μ -CT=0.01 mm³, NT=0.03 mm³. The width of the samples is approximately 4.5 cm. Owing to the manner in which the samples were mounted, the lowest sections of the PB and CB samples were omitted during the μ -CT imaging

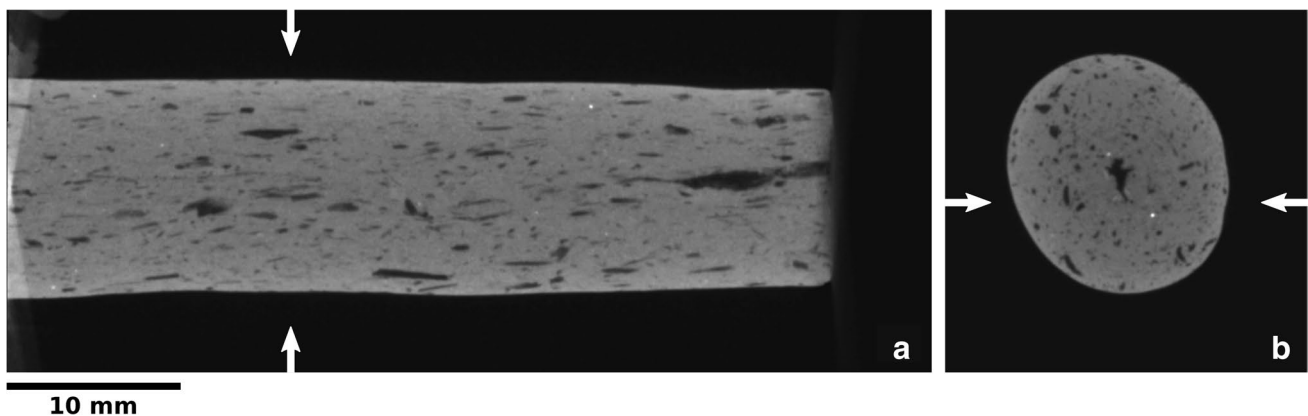
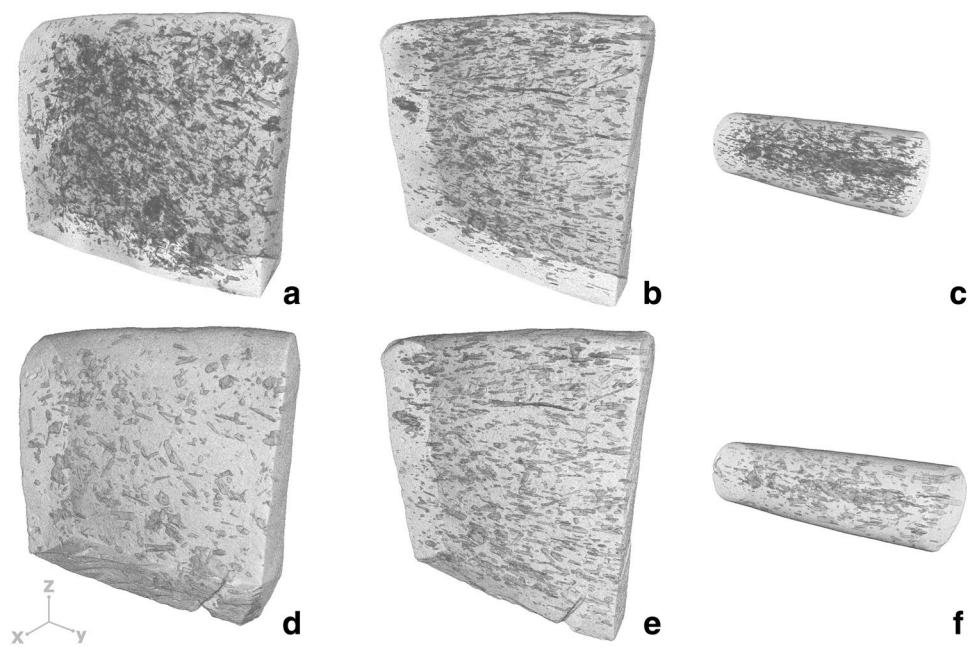


Fig. 7 μ -CT 2D tomographic planar slices of Co1: **a** horizontal/tangential section; **b** vertical section. The corresponding locations of planes are indicated by arrows. As also shown in the 3D models (Fig. 6), the objects are preferentially aligned in the direction of the length of the coil. Consequently, the particles of fibrous dung temper (and/or corresponding relic voids) are seen as comparatively large

elongated shapes in **a**, whereas they are seen as smaller, more equidimensional shapes in **b**. The vertical planar cross-sectional view (**b**) differs significantly from the 2D schematic diagram and radiographic projection views shown respectively by Rye (1977, plate 3) and Berg (2008, fig. 5)

objects in the cross-sectional views, which in the respective illustrations presented by Rye (1977, plate 3a) and Berg (2008, fig. 5) appear to align parallel to tangents to the circumference of a coil, or in a spiral pattern. Such apparent orientations of objects as described by Rye and Berg could only be seen with the cumulative effect of radiographic projections, as discussed above, where through foreshortening the size, shape, and orientation of objects in 3D space is distorted as it is projected onto 2D images (e.g. a long object approximately aligned to the length of the coil, appears in a 2D vertical projection as a shorter object aligned to the

circumference of the coil). Consequently, when depicting the orientation of objects in schematic diagrams, it is important to clarify whether these depict their appearance in planar 2D sections or cumulative 2D projections. In this regard, the appearance of objects in coils and coil-built vessels when viewed in planar thin sections or fresh fracture cross-sections (e.g. Fig. 3) will not correspond to that seen in schematic diagrams seemingly based on radiographic images (e.g. Berg 2008, fig. 1; Rye 1977, plate 3), but rather will more closely resemble that seen in the tomographic slices presented here (Figs. 7–8, see also Online Resource 1).

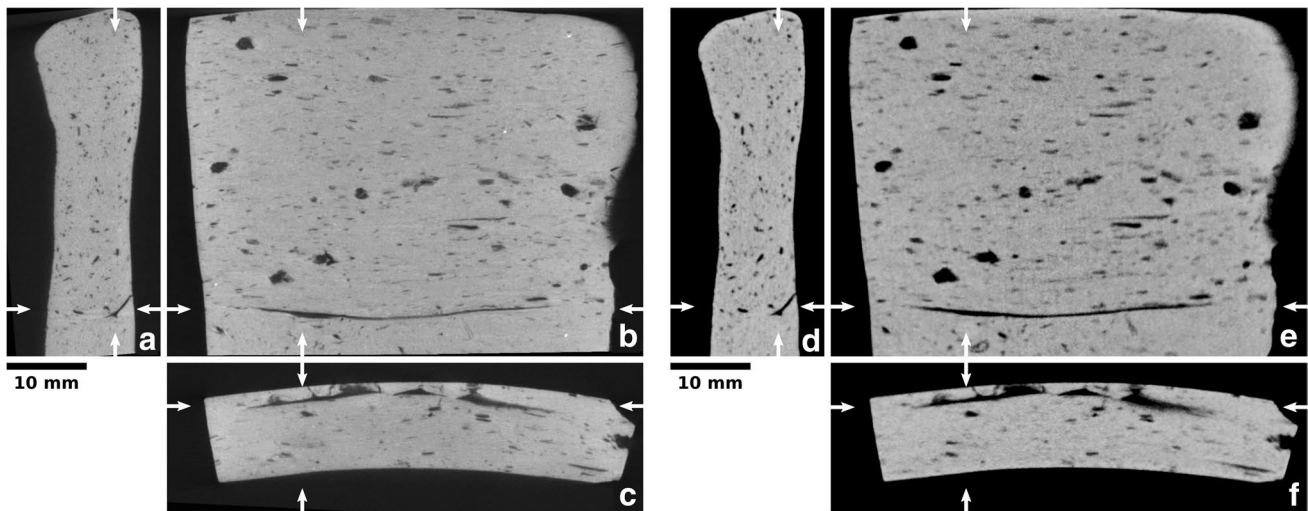


Fig. 8 Matching μ -CT (a–c) and NT (d–f) tomographic slices of CB3 showing, towards the base of the sample, a visible separation between successive coil layers: **a** & **d** vertical slices, **b** & **e** tangential slices, **c** & **f** horizontal slices. The locations of corresponding planes aligned through the feature are indicated by arrows. While one boundary

between coil layers is visible in both μ -CT and NT towards the base of the sample, the joins between the other three or four layers of coils are not visible, thereby indicating the difficulty of consistently identifying coil-building from such macro-structural features

Another feature to emerge from both the μ -CT and NT imaging of the CB samples was the scarcity of detected coil joins. From the height of the CB samples relative to the diameter of the constituent coils, each sample was made from approximately four or five layers of coils, resulting in three or four joins between coils. However, in practice, typically only one boundary between coil layers was visible in each of the three CB samples, and even in these instances they were not readily identifiable throughout the thickness of each sample (Figs. 8–9, see also Online Resource 1). This apparent scarcity and variability of discernible coil joins within all three of the CB samples highlights the general difficulty of relying on such macro-structural features to consistently identify the use of coil-building techniques (contra e.g. Carr 1990, pp. 16–17; Middleton 2005, p. 85), especially when examining sherds rather than complete vessels.

Determination of nature of segmented objects

From examinations of fresh breaks and thin sections, it was known that the fired samples did not contain aplastic inclusions of sufficiently large size to be detected by μ -CT or NT in the instrument configurations used in the present study, and that the cattle dung temper was (in most instances) completely burnt away leaving relic voids, or else remained as carbonised particles (especially in the core) (see Fig. 3). Owing to the low attenuation of X-rays by organic materials, it was known that such carbonised particles would be largely indistinguishable from voids in the μ -CT imaging; however,

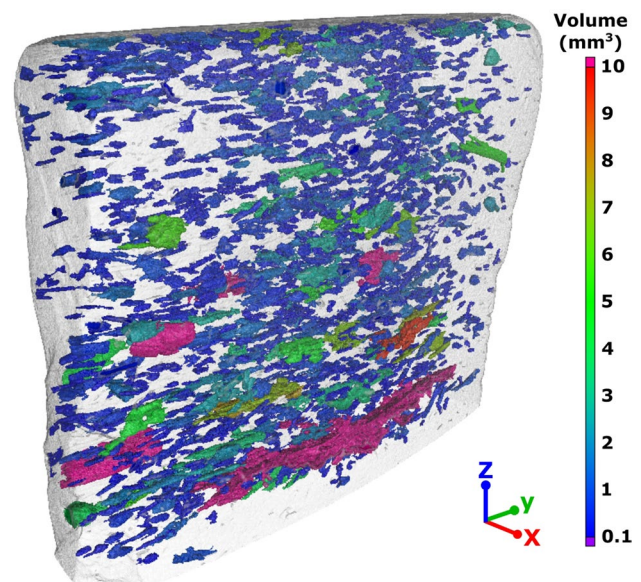


Fig. 9 Segmented 3D μ -CT model of CB3, showing objects greater than 0.1 mm³ coloured according to volume. A large void (coloured magenta) towards the base of the sample represents a discontinuity between two layers of coils, and corresponds to the large void seen in the orthogonal 2D tomographic slices shown in Fig. 8. Although other large-volume features are also seen in the 3D model, they are difficult to confirm as necessarily reflecting boundaries between layers of coils

as discussed above, it was less certain how the same particles would appear in NT imaging, where the potential presence of high neutron attenuating ¹H might result in a clear separation of residual organic particles from voids.

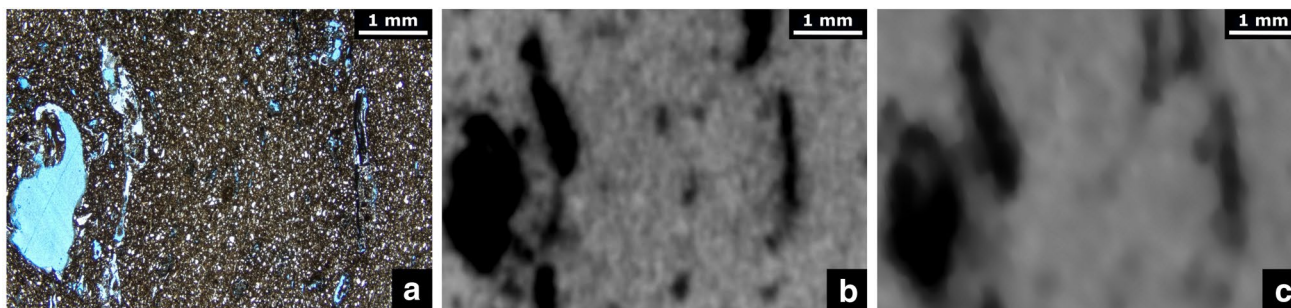


Fig. 10 Approximately matching horizontal sections of PB1 after initial firing: **a** photomicrograph of a petrographic thin section ($\times 20$, PPL); **b** μ -CT slice; **c** NT slice. The planes of the tomographic slices were adjusted manually to match the thin section plane. Larger voids (stained blue, left) and carbonised particles (elongated and opaque, right) seen in the thin section both appear as black or dark grey objects in the μ -CT and NT slices, indicating that in both imaging

The compositions of the segmented objects detected by tomographic imaging were therefore determined in two ways: through visual comparisons between tomographic slices and thin sections made in the same planes, and by statistical comparisons between the distributions of objects detected in the NT imaging of fired and refired samples.

Figure 10 shows details from vertical μ -CT and NT tomographic slices approximately matched to a vertical thin section from a sample as initially fired. As the thin section was prepared after the initial tomographic imaging had been completed, it was possible to extract tomographic slices corresponding to the same plane as the thin section (although, in practice, as this required manual manipulation of the 3D models, finding exactly matching planes was difficult). The thin section photomicrograph shows areas of voids (stained blue) together with elongated particles of carbonised cattle dung. In the corresponding details from the μ -CT slice, the larger voids and carbonised particles both appear as black objects indicating a similar, although not necessarily exactly the same, low level of X-ray attenuation. In the NT slice, the same features also appear black or dark grey, indicating a similar lack of differentiation between voids and carbonised particles. Furthermore, in the latter image, the absence of bright white features, as would be expected for areas of high neutron attenuation, indicates that the carbonised organic inclusions do not retain sufficiently high concentrations of ^1H to be detected by NT.

The above example appears to indicate that in both μ -CT and NT residual, carbonised, organic particles display similar greyscale values to voids. However, owing to beam hardening effects (wherein, as a result of the preferential attenuation of lower energy components, the mean energy of an incident radiation beam increases as it progresses through a sample), it is not possible to make a simple direct correlation

modalities voids and carbonised particles display low X-ray and neutron attenuations. Consequently, both types of objects appear not to be differentiated from each other in μ -CT and NT. In the NT slice, the absence of areas of high neutron attenuation (which would appear as bright white objects) in the vicinity of the carbonised particle also indicates that such particles do not show the high attenuation otherwise expected for unfired organic materials

between greyscale values and composition. Nonetheless, as the features in the above example are in close proximity to each other, the effect of beam hardening may be regarded as minimal.

Further evidence for how carbonised particles were detected by NT imaging was provided by comparing the distributions of the segmented data from the same samples before and after refiring (i.e. the distributions of objects determined for the same samples obtained after the initial firing, and again after a second firing). It was assumed that if carbonised particles were differentiated from voids in NT, then there would be a noticeable difference between the fired and refired samples in the size and frequency of the objects detected following the removal of carbonised particles during refiring. From macroscopic observations of the samples, it appeared that, as intended, the refiring process resulted in the complete removal of the partially combusted particles that had remained in the cores after the initial firing. The refired samples were imaged by NT and the resulting data processed in the same manner as previously undertaken following the initial firing of the same samples.

The distributions of the lengths (L in Fig. 5a), of the objects in the fired and refired samples were compared using the Kolmogorov-Smirnoff nonparametric test (with a significance level of 5%). As shown in Fig. 11a, b the lengths of the objects appear visually to follow very similar distributions; an impression which is confirmed by the results of the Kolmogorov-Smirnoff tests (Fig. 11c, d) with values of $p = 0.723$ and $p = 1.000$ values respectively for CB1 and PB1.

These results confirm the observations made from the above visual comparisons of tomographic slices and thin sections that, in both μ -CT and NT, partially combusted organic inclusions are not substantially differentiated from voids. On the one hand, this finding indicates that NT does

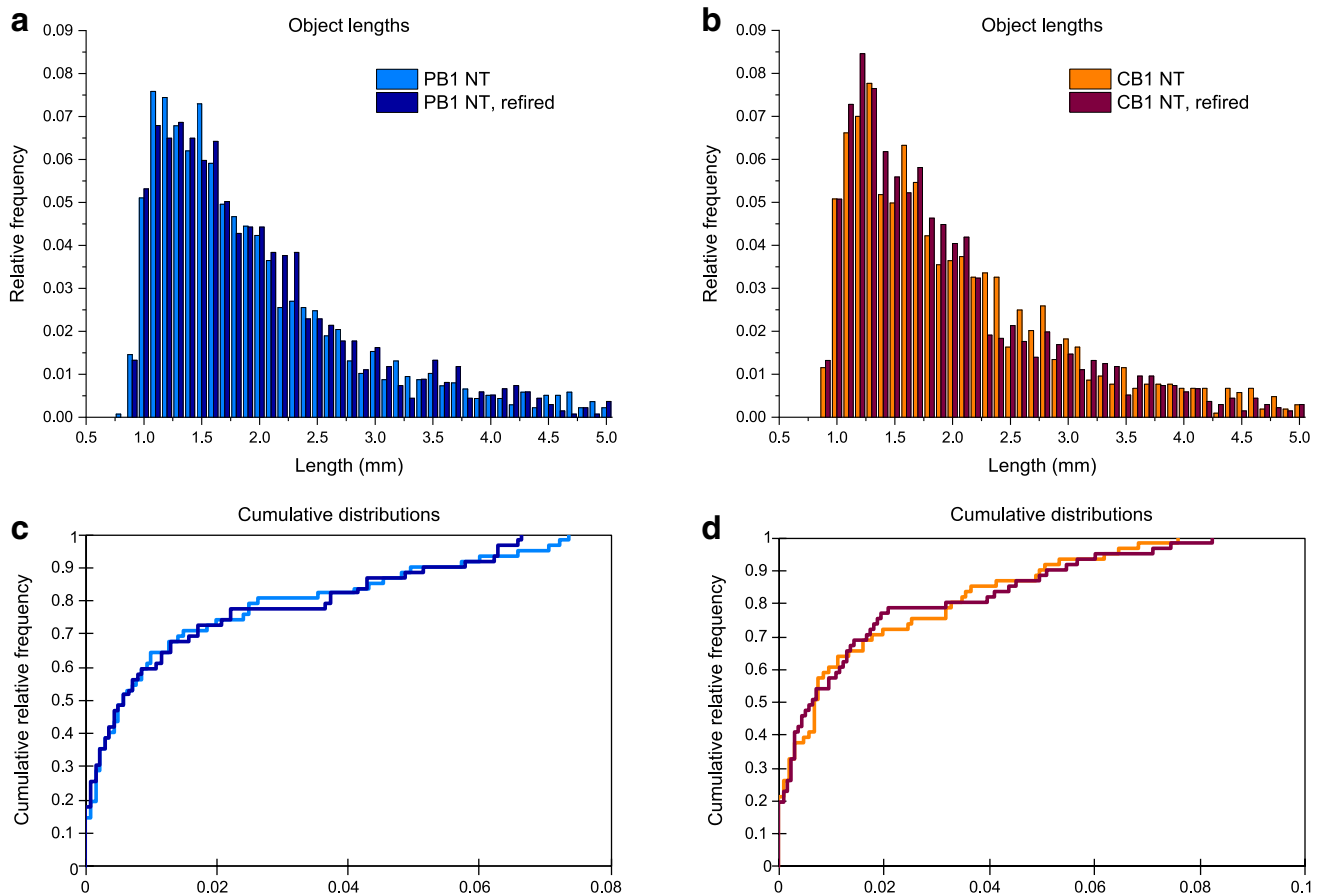


Fig. 11 Comparison of object lengths in NT between the fired and refired samples. The frequencies of objects are normalised due to the smaller size of the refired samples (and hence smaller absolute number of objects) following removal of thin sections after initial firing. **a**

& **b** Relative frequency distributions of the lengths of objects for CB1 and PB1 respectively; **c** and **d** cumulative relative frequency curves of CB1 ($p=0.723$) and PB1 ($p=1.000$), respectively, used in the Kolmogorov-Smirnov tests

not offer any greater sensitivity over μ -CT in the detection of organic tempers in fired pottery; however, on the other hand, it suggests that the two imaging techniques are more directly comparable in that, despite differences their modes of operation, they nonetheless detect voids and fired organic inclusions in similar manners.

The grouping of organic particles and relic voids by μ -CT and NT necessitates some additional considerations with regard to subsequent analyses and interpretations of the datasets of segmented objects. In the first instance, this grouping may be considered an advantage in that all of the organic inclusions may be analysed together regardless of the vagaries of firing conditions that result in some particles being fully combusted and others carbonised. Conversely, it also prevents investigation of what may be intentional technical differences in firing practices. Additionally, there is a complication in terminology, with organic inclusions in fired samples consisting of both solid, carbonised particles as well as relic voids; owing to such ambiguity, the term ‘object’, as initially defined above, may still be used to refer

to individual segmented elements irrespective of their composition or origins. Nonetheless, with regard to the determination of forming techniques through the orientation of objects, relic voids from combusted organic temper may be considered as particles, as their orientations were set during forming processes while still solid particles, prior to firing.

Of potentially greater difficulty, however, is the indiscriminate amalgamation of objects representing temper and ‘true voids’ (i.e. voids that were present within the unfired, but formed, vessels) within the segmented datasets. Consequently, voids originating as air pockets or structural discontinuities are grouped together with particles and relic voids of organic temper and non-temper organic inclusions, as well as with inclusions of other low attenuating materials. Some differentiation of these categories of objects may be achieved by size and shape filters (e.g. volume, sphericity, compactness, length, aspect ratio), although these necessarily require some prior knowledge of the approximate appearance of different materials (which, for archaeological pottery, may not be evident), and do not necessarily ensure

a correct separation of materials according to their original compositions (e.g. an elongated gaseous void may be indistinguishable by shape or size from a fibre of dung temper). However, while such uncertainties may be unsatisfactory, they need not necessarily preclude the differentiation of forming techniques; and, as a pragmatic solution to this goal, the orientation of *all* particles and voids, regardless of whether they originate as temper, may be utilised.

While it has been shown that organic particles and voids are detected in similar manners in both μ -CT and NT, the datasets generated in each imaging modality for each sample are not necessarily identical. Differences in the specific objects detected arise largely from differences in the maximum spatial resolutions of the instruments, but also from differences in the thresholding parameters used to isolate objects from sample matrices during image processing. The latter may vary both from sample to sample, but also between imaging modalities, in response to various factors, such as sample thickness and beam hardening. However, while there may be some differences in the specific objects included within the datasets generated by μ -CT and NT, the distributions of various parameters of each dataset remain statistically very similar (as demonstrated below).

Results and discussion of the quantitative 3D analysis

For each sample, in both μ -CT and NT, a large quantity of data was generated regarding the volume, aspect ratio, projected sizes, and polar coordinates of the objects, as well as the corresponding means and OIs (see Online Resource 2 for full, unfiltered datasets). Using this information, statistical analyses were performed on the filtered datasets of objects for each sample, examining specifically whether differences in the OIs and mean polar coordinates corresponded to differences in forming techniques and/or imaging modality. Robustness analysis (RA) was also applied to each metric to determine the strength of the results with regard to changes in initial parameters.

Projected sizes

The relative frequency distributions of the lengths (L in Fig. 5a) and projected sizes of objects, in μ -CT and NT, are shown in Figs. 12–13 using CB1, PB1, and Co1 as examples (see Online Resource 3 for similar charts for the other samples). In Fig. 12, similar length distributions are seen for all three samples, in each imaging modality, suggesting that differences in forming technique did not affect the lengths of the objects. The slight initial offset between the distributions in μ -CT and NT may be accounted for by differences

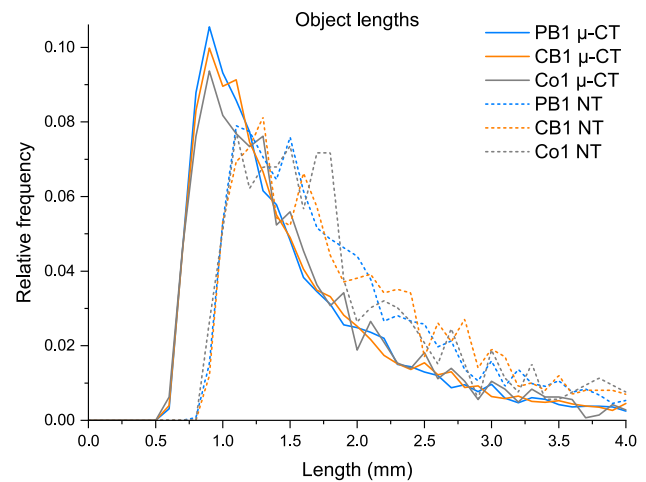


Fig. 12 Relative frequency distributions of the maximum lengths (L) of objects in the filtered datasets from CB1, PB1, and Co1, in μ -CT and NT, in 0–4 mm range. Within each imaging modality, similar length distributions are seen for all three samples indicating that differences in forming technique did not affect the lengths of the objects. The slight initial offset between the μ -CT and NT distributions reflects the different minimum voxel limits of the respective datasets, resulting from the difference in the spatial resolutions of the imaging systems. The smaller number of objects in the NT datasets compared to the corresponding μ -CT datasets (by around one order of magnitude) results in larger uncertainties in their relative frequencies, reflected here in the greater fluctuation of the curves. For ease of visualisation, the histograms for each sample are plotted as lines, with the plotting points taken as the midpoint of each, equally spaced, length bin. See Online Resource 3 for comparable results from additional samples

in the spatial resolutions of the instruments, indicating that, as expected, NT detected proportionally fewer small objects than μ -CT, thereby also exaggerating the relative proportion of large objects.

In Fig. 13, however, differences can be seen between the forming techniques in the relative frequency distributions of the projected sizes of the objects. In both imaging modalities, the x -axis projections follow very similar relative frequency distributions for all three samples. For the y -axis projections, CB1 and Co1 follow similar distributions, while for PB1 there is a shift towards lower values; but the most visible differences are seen in the z -axis projections, where CB1 and Co1 again follow similar distributions to each other (and also similar to their corresponding x -axis distributions), but the distribution of PB1 is shifted towards larger values.

These figures indicate that, overall, the objects are distributed in a similar manner in CB1 and Co1, but differ substantially in PB1. The tendency in both CB1 and Co1 for small value z -axis projections and large y -axis projections indicates that the objects lie close to the y -axis in these samples. Furthermore, for both of these samples, the similarity of the x -axis and z -axis projections indicates that the objects are also symmetrically distributed about the y -axis. This

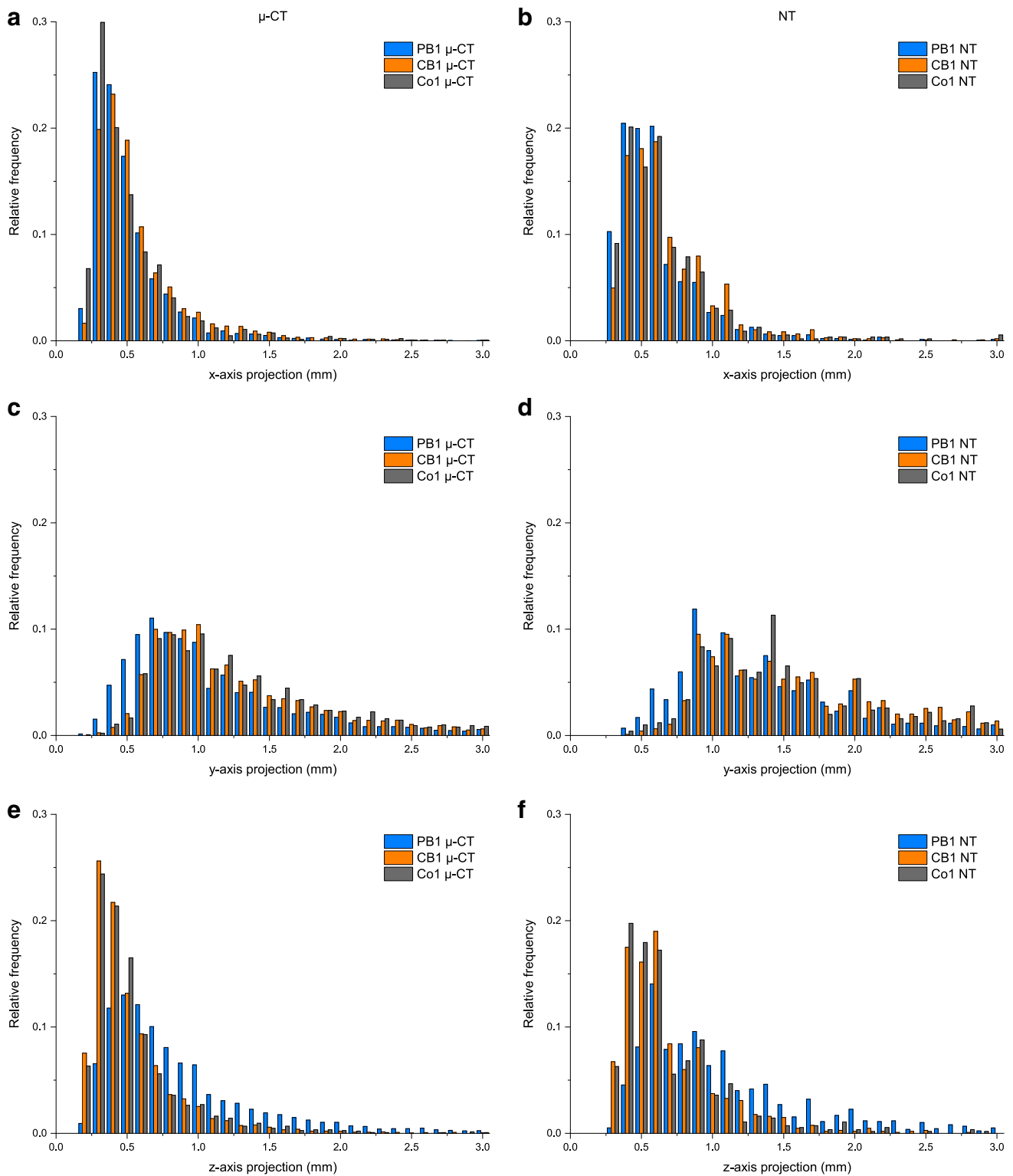


Fig. 13 Relative frequency distributions of the projected sizes of objects in the filtered datasets from PB1, CB1, and Co1 in μ -CT (**a**, **c**, **e**) and NT (**b**, **d**, **f**), in the range 0–3 mm. In both imaging modalities, CB1 and Co1 follow similar distributions to each other in each

axis, while PB1 is clearly differentiated in y-axis and z-axis projection distributions. See Online Resource 3 for comparable results from additional samples

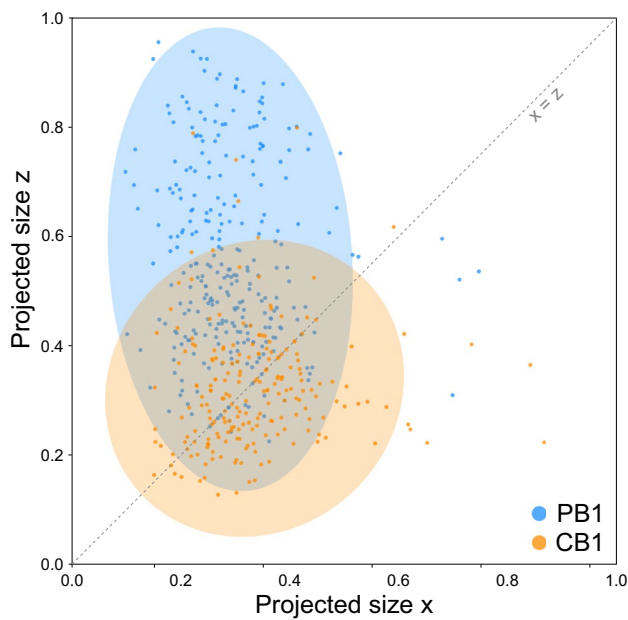


Fig. 14 Scatter plot of pairs of corresponding x - and z -axis projections of objects in filtered NT datasets from PB1 and CB1. The projected size values were normalised with respect to the length (L) of the objects. Ellipses correspond to 95% estimated concentration of samples. For ease of visualisation, and owing to the very large number of objects within each dataset, only 1 in 5 objects from the smaller NT datasets (when sorted by volume) is plotted. Similar patterns are also seen when using CT datasets

symmetrical behaviour is further illustrated in Fig. 14, in which corresponding pairs of x - and z -axis projections from CB1 are approximately symmetrically distributed about the

line $x=z$; by contrast objects from PB1 display an asymmetrical distribution. Such near symmetrical distribution of objects about the y -axis in CB1 and Co1 seemingly arises from the near-even distribution of forces during the rolling of the coils, and also indicates that in CB1 the process of joining coils did not significantly change the overall orientation of the objects as previously obtained during the preceding preparation of the coils themselves.

For PB1, the objects display a different pattern of orientation than that seen in CB1 and Co1. For PB1, in both imaging modalities, the z -axis projections tend towards larger values than they do for the other two samples, indicating that in PB1, the objects lie closer to the z -axis. However, unlike CB1 and Co1, for PB1, the z - and y -axis projections follow a broadly similar distribution, albeit with a slight tendency towards larger y -axis projections (Fig. 15). The approximate similarity of these two distributions indicates that the objects tend to be symmetrically distributed about the x -axis. A lack of preferential orientation in the tangential plane (i.e. in the y - z plane) has previously been suggested as indicative of percussion-building techniques (e.g. Rye 1981), and even within the present study it is difficult to discern visually any preferential orientation of the objects in tangential tomographic slices of PB1 (Fig. 16). Nonetheless, the quantitative analysis of the objects in PB1 (and also PB2 and PB3) shows an unexpected, but discernible, tendency for slightly larger values in the y -axis indicating that the objects tend to be preferentially inclined towards the y -axis rather than the z -axis (although not to the same extent as seen in CB1 and Co1). A possible explanation for this observed phenomenon may be found in the broad,

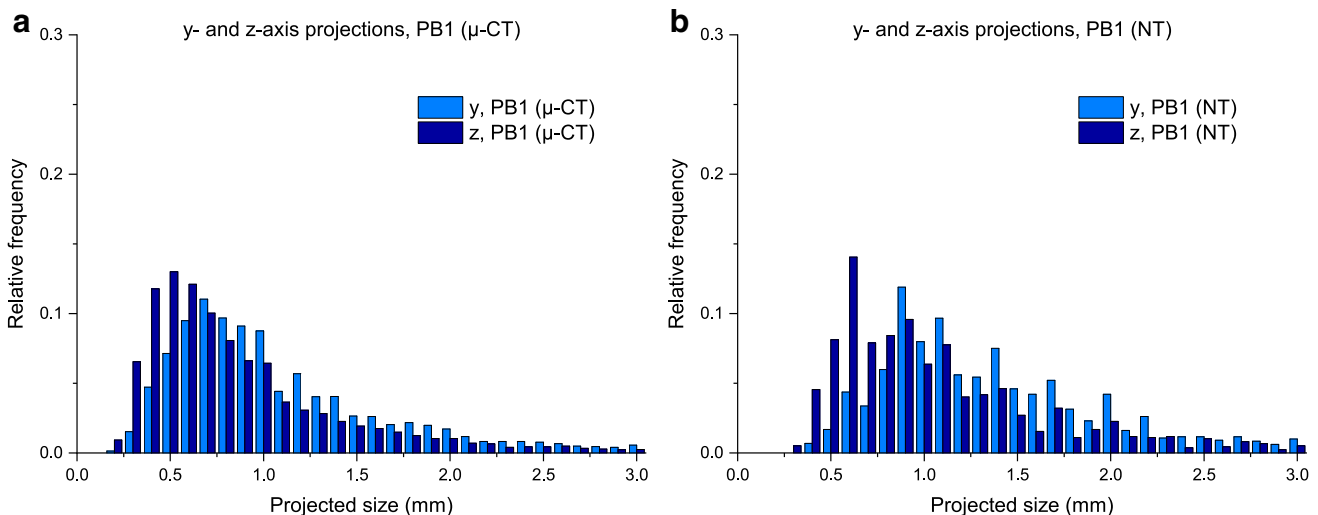


Fig. 15 Relative frequency distributions of the projected sizes of objects in the filtered datasets from PB1 in μ -CT (a) and NT (b), in the range 0–3 mm. In both imaging modalities, there is a slight tendency for larger values for y -axis projections. This sample illustrates

that, contrary to previous expectations, vessels made using percussion-building techniques may display subtle preferential orientations of objects in tangential planes (i.e. y - z planes)

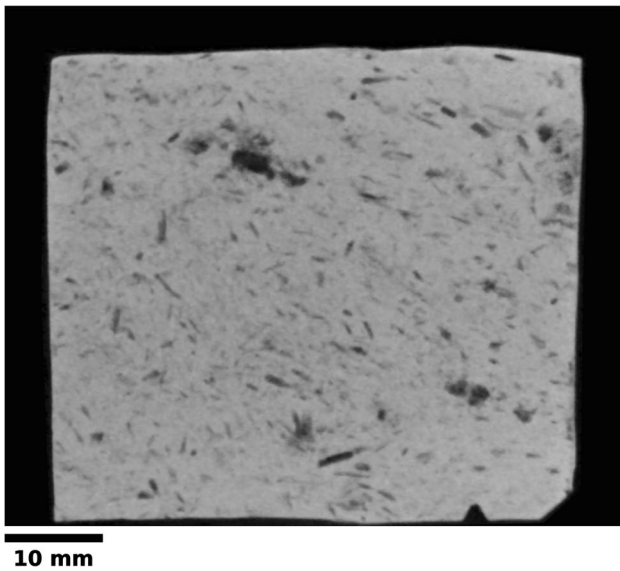


Fig. 16 NT tangential tomographic slice of PB1. From visual inspection, it is difficult to discern any preferential orientation of the objects towards either the *y*- or *z*-axes; however, from the evaluation of the projected sizes of the segmented and filtered objects from the entire 3D tomographic model, a slight preferential alignment towards the *y*-axis can be detected

open vessel shape of PB1, where the diameter exceeds the height (30.5 and 8.5 cm respectively). In order to achieve this shape during forming, clay from the initial unformed body must have been moved more in a lateral direction (i.e. in the *y*-axis), in order to increase the diameter of the vessel, than it was moved vertically (i.e. in the *z*-axis), to increase the height of the vessel. Such asymmetric movement of clay during forming further suggests that the percussive forces were not applied strictly perpendicular to the vessel walls (as previously described above) but rather at a slight inclination. In the TCA forming technique, an inclined resultant force may have been achieved through the positioning of the vessel, and by the potter’s vertical striking action impacting against the wall of the vessel when held adjacent to the sides

of the curved depression in the ground, rather than at the base of the depression.

Orientation Index (OI)

The examples of CB1 and PB1 suggest that forming techniques may be discriminated by differences in the relative frequency distributions of the projected sizes of objects, using data from either μ -CT or NT. A more general way of comparing samples using potential differences in the projected sizes of objects is provided by the Orientation Index.

Table 1 shows the calculated OI and its uncertainty for each sample, using the projected sizes of the segmented objects from the filtered μ -CT and NT datasets. The table shows that CB and Co samples display similar near-zero values, whereas the PB samples display consistently higher values. In other words, when the projected sizes of the objects are normalised with respect to the longest projected dimension (in these instances, the *y*-axis projection), there is a very stable behaviour in the relative length of the two other projected sizes according to whether they were made by coiling or percussion-building. This result applies to both μ -CT and NT, suggesting that as a unit of measure OI may readily facilitate comparisons between different imaging modalities and instruments.

Not only do these results suggest that the OI may be used to differentiate vessels made using coil- and percussion-building techniques, but the similarities in the values of OI for both the CB and Co samples again indicate that most of the objects became orientated during the rolling of the coils. Moreover, in the samples analysed here, the process of joining successive layers of coils during coil-building appears not to have resulted in a significant overall change in the alignments of the objects in the preformed coil sections. While it is likely that some particles near the surfaces of the CB samples may have become reoriented, they seemingly constituted only a small proportion of the

Table 1 Calculated Orientation Indices (OI) for percussion-built (PB) and coil-built (CB) samples, and coil section samples (Co), from the filtered μ -CT and NT datasets (uncertainty calculated by error propagation from the standard errors (SE) of the normalised *x*-axis and *z*-axis projections)

Sample	Object frequency		Orientation Index μ -CT		Orientation Index NT	
	μ -CT	NT	OI	Unc	OI	Unc
PB1	6657	1423	0.36	0.01	0.38	0.02
PB2	7741	1141	0.28	0.01	0.30	0.02
PB3	7937	909	0.25	0.01	0.27	0.02
CB1	7340	1069	0.03	0.01	0.00	0.01
CB2	6650	1455	0.07	0.01	0.03	0.01
CB3	5175	883	0.01	0.01	0.04	0.02
Co1	1488	558	0.02	0.01	0.03	0.02
Co2	1536	530	0.03	0.01	0.00	0.02
Co3	1140	415	0.06	0.02	0.05	0.03

total number of objects detected, and therefore had a negligible influence on the OI values.

Robustness analysis of Orientation Index

While clear differences between coil- and percussion-based forming techniques may be seen in the measured OI values for the samples in Table 1, further investigation of the strength of these results can be achieved through robustness analysis. RA examines the extent to which changes in certain parameters may influence the results, and consequently whether the results measured from a comparatively small number of samples might be expected to be repeated with a larger assemblage.

To provide input data necessary for the RA, the distributions of the parameters (volume and aspect ratio) suspected as being influential on the OI were first normalised,

and then compared with regard to forming technique and imaging modality. As can be seen in Fig. 17, within each imaging modality, the distributions of both parameters are almost identical across the three sample series, indicating that the primary forming techniques did not differentially affect the volume or aspect ratio distributions of the temper; a slight difference is present in the distributions of aspect ratio for Co compared to CB and PB, but for the purposes of RA this is judged to be negligible. Consequently, as volume and aspect ratio both appear not to be influenced significantly by forming techniques themselves, they can be used to measure the effects of the forming techniques on the orientation of the objects. However, as shown in Fig. 18, more significant differences are present in the normalised frequency distributions of both parameters when comparing μ -CT and NT, largely due to differences in the minimum size of objects detected by each

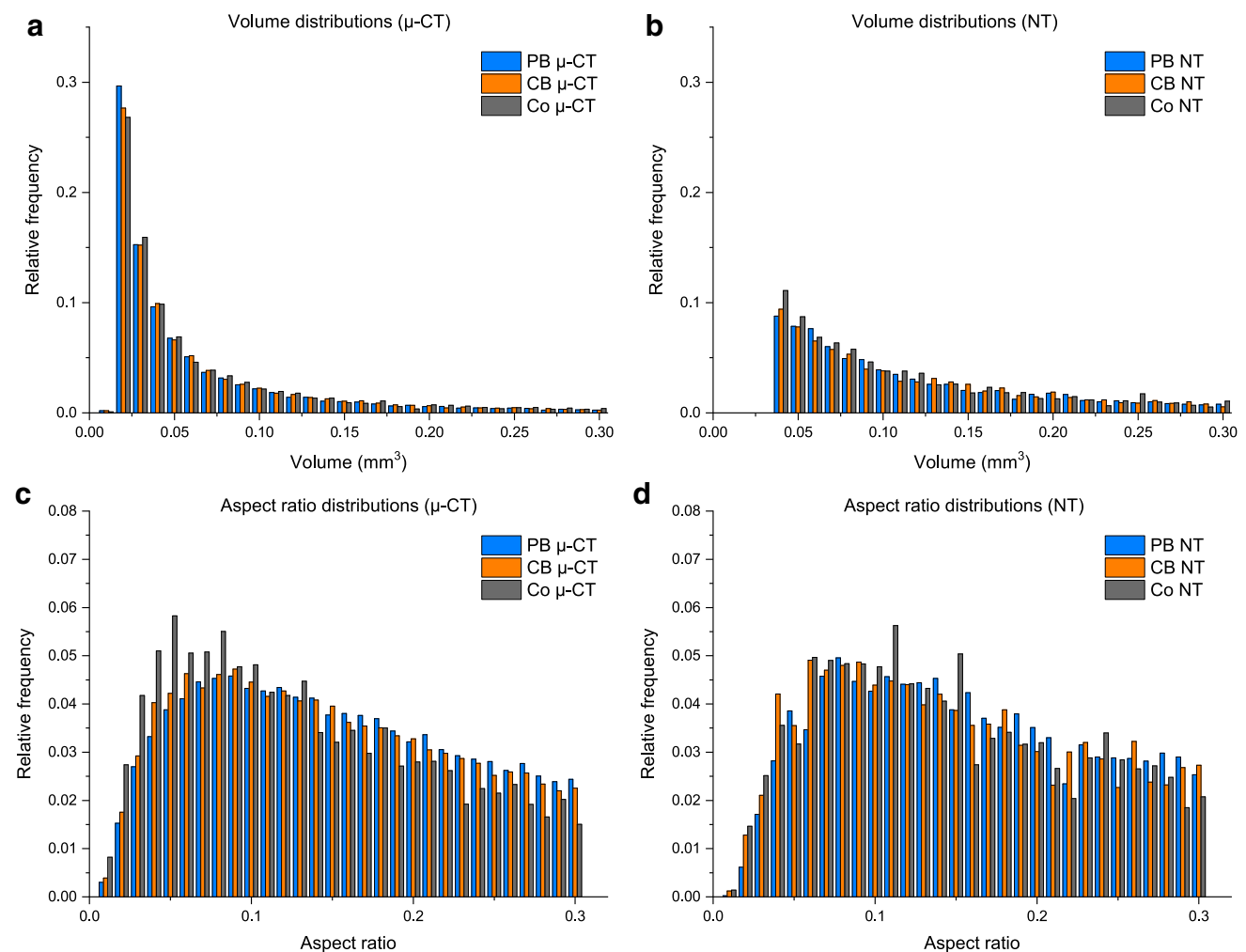


Fig. 17 Relative frequency distributions of volume (a–b), and aspect ratio (c–d) of objects in PB, CB, and Co samples as averaged over the three samples in each series, from filtered μ -CT and NT datasets. The

similarities in the distributions indicate that volume and aspect ratio were not substantially influenced by differences in forming techniques

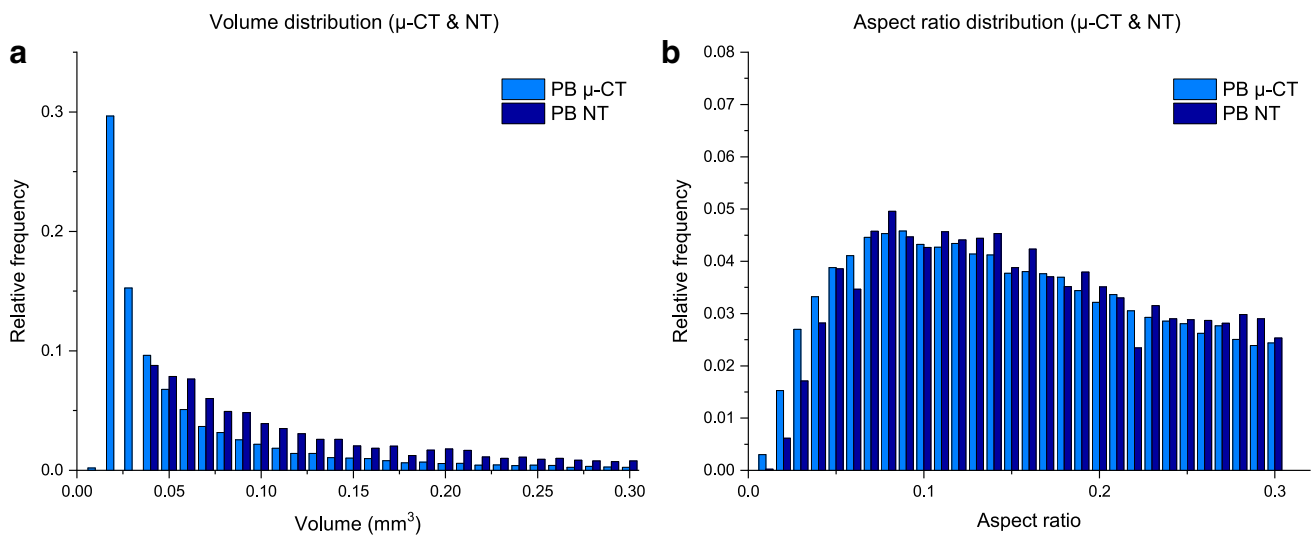


Fig. 18 Relative frequency distributions, averaged from PB1, 2, and 3, for volume (a) and aspect ratio (b) of objects from filtered μ -CT and NT datasets. The distributions differ in shape between imaging modalities, therefore requiring both parameters to be sampled separately for the RA

technique; therefore, the RA must be performed separately for both imaging modalities. Accordingly, a total of four distributions were calculated for the RA representing two imaging modalities (μ -CT and NT) and two parameters (volume and aspect ratio).

For the next stage of the RA, it was necessary to determine the input correlation matrix for the parameters, for which Spearman’s rank correlation coefficients were used, calculated separately for the filtered μ -CT and NT datasets. For both imaging modalities, the correlation matrices showed very weak negative correlations (-0.08 and -0.19 for μ -CT and NT respectively) between volume and aspect ratio.

The results of the RA are given in Table 2. From this, it can be seen that for both μ -CT and NT, the mean values for the OI from 5000 simulations are near zero for both the CB and Co simulations, whereas for the PB simulations, it is approximately 0.32. These values are similar to those directly measured from the samples themselves (Table 1). Moreover, there is a significant difference in the mean values of the OI from the RA simulations between forming techniques, as the confidence intervals of the means of the CB and PB simulations do not overlap at $\text{mean} \pm 2 \times \text{SD}$ (i.e. a 95% probability). Importantly, however, the standard error values (SE, which here refers to the SD of the mean values

and not the SD of the simulations themselves) for the mean values from the simulations are also consistently very low, demonstrating the extreme stability of the OI metric. Therefore, the results of the RA simulations not only closely agree with the OI values directly measured from the samples, but also demonstrate a high stability in these values, indicating that the OI metric is very well suited to distinguishing coil-based techniques from percussion-building techniques.

Polar and azimuth angles

In a similar manner to projected sizes and the OI, potential differences between forming techniques can also be expressed in terms of the polar (θ) and azimuth angles (ϕ) of the segmented objects. Relative frequency distributions of θ and ϕ from μ -CT and NT are shown in Figs. 19–20 using PB1, CB1, and Co1 as examples (see also Table 3 and Online Resource 3). From these figures, it can be seen in both imaging modalities that the shapes of the relative frequency distributions of θ and ϕ are similar for CB1 and Co1, but clearly differ for PB1.

For CB1 and Co1, the polar angles of the objects follow narrow, positively skewed log-normal, or near log-normal, distributions with means of 17° and 16° respectively (averaged across μ -CT and NT); in PB1, while the polar angle

Table 2 Statistical results of RA of Orientation Indices (OI), using 5000 simulations of filtered μ -CT and NT datasets

	OI μ -CT			OI NT		
	Mean	SD	SE	Mean	SD	SE
PB	0.31	0.02	0.00	0.33	0.03	0.00
CB	0.03	0.00	0.00	0.02	0.01	0.00
Co	0.03	0.01	0.00	0.02	0.01	0.00

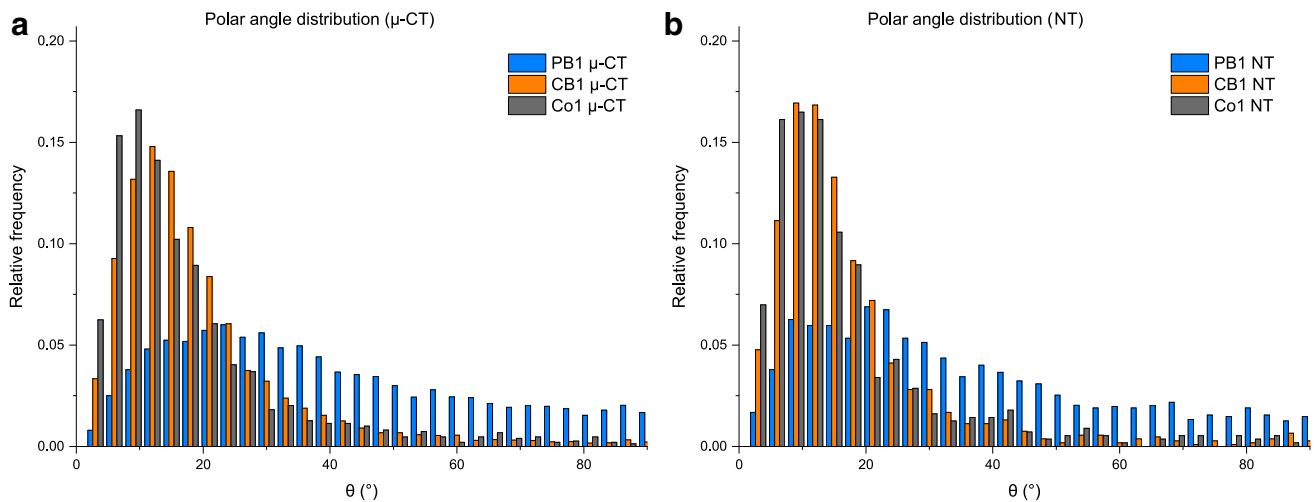


Fig. 19 Relative frequency distributions of polar angles for PB1, CB1, and Co1, from filtered μ -CT (a) and NT (b) datasets. In both imaging modalities, the distributions of PB1 clearly differ from those of CB1 and Co1. The slight difference between CB1 and Co1 may be

distribution is also best described by a near log-normal distribution, the shape is substantially broader, and with a mean θ of 36° (averaged across μ -CT and NT). For the azimuth angle distributions, in both μ -CT and NT, the situation is largely reversed, with objects in PB1 displaying a narrow distribution, grouped closely around 90° (mean of 87° across μ -CT and NT), while CB1 and Co1 display considerably broader, near-uniform, distributions.

However, unlike for θ , the mean values of ϕ for CB1 and Co1 (166° and 115° respectively across μ -CT and NT) do not agree closely with each other, although they display similarities in the general shapes of the azimuth angle distributions. This lack of agreement of the mean ϕ values is due to the variability of the statistic in Co1 (and all Co samples), which varies according to the rotational position of the sample (see Online Resource 4); for Co1, there is no single ‘correct’ sample positioning around the y -axis, unlike for CB1 where the rotational position is defined by the walls of the sample. Nonetheless, when considering vessel samples, CB1 and PB1 are clearly distinguished from each other by the shapes of the angle distributions, as well as by the differences in the mean values of θ and ϕ , and in the standard deviations of ϕ .

The statistical distributions of θ and ϕ may be interpreted in terms of general tendencies in the appearance of objects seen within all the experimental samples, achieved in response to the forces applied during different forming techniques. For both CB and Co samples, the objects tend to lie closer to the y -axis (i.e. smaller θ), than they do in PB samples, but are also more uniformly distributed around the y -axis (i.e. large CSD in ϕ distribution), indicating little preferential orientation of objects towards

due to the differences in the curvature of the samples, where CB1 was curved according to the curvature of the vessel walls, whereas Co1 was straight

either the x - or z -axes, although a slight tendency towards ϕ values closer to 180° can be seen in the CB samples (mean of 160° , averaged across μ -CT and NT). This pattern accords with the expectation that during the preparation of coils, particles and voids became more aligned to the length of the coil as the initial clay mass was increasingly drawn out, and θ may have decreased further as the length of the coils increased (with a corresponding decrease in coil diameter). Similarly, the near-uniform distribution of ϕ may be interpreted as resulting from forces being applied equally around the circumference of the coil as it was rolled. However, slight but unequal compression of the coils during forming, giving coils roughly elliptical cross-sections, resulted in a slight tendency for the objects to additionally align towards the longer of the two cross-sectional axes (i.e. perpendicular to the direction of the resultant compression of the coil, but independently of the θ distribution; see Online Resource 4).

In the Co samples, this slightly uneven distribution of objects around the y -axis resulted in large differences in the mean ϕ , varying according to the rotational position of each sample when analysed. For the CB samples, however, the mean ϕ appears more stable, commonly displaying values close to c. 160° , which in turn may represent a subtle technological variant within the range of coil-building practices, and a consistent forming practice of the potter that made all three CB vessels. In general, mean ϕ values less than 45° from either the positive or negative x -axis (i.e. in the ranges 0 – 45° or 135 – 180° and their equivalent axial values) appear to reflect the overall vertical compression of coils as successive layers are vertically pressed together during the coil-building process (i.e. compression in the z -axis). Depending

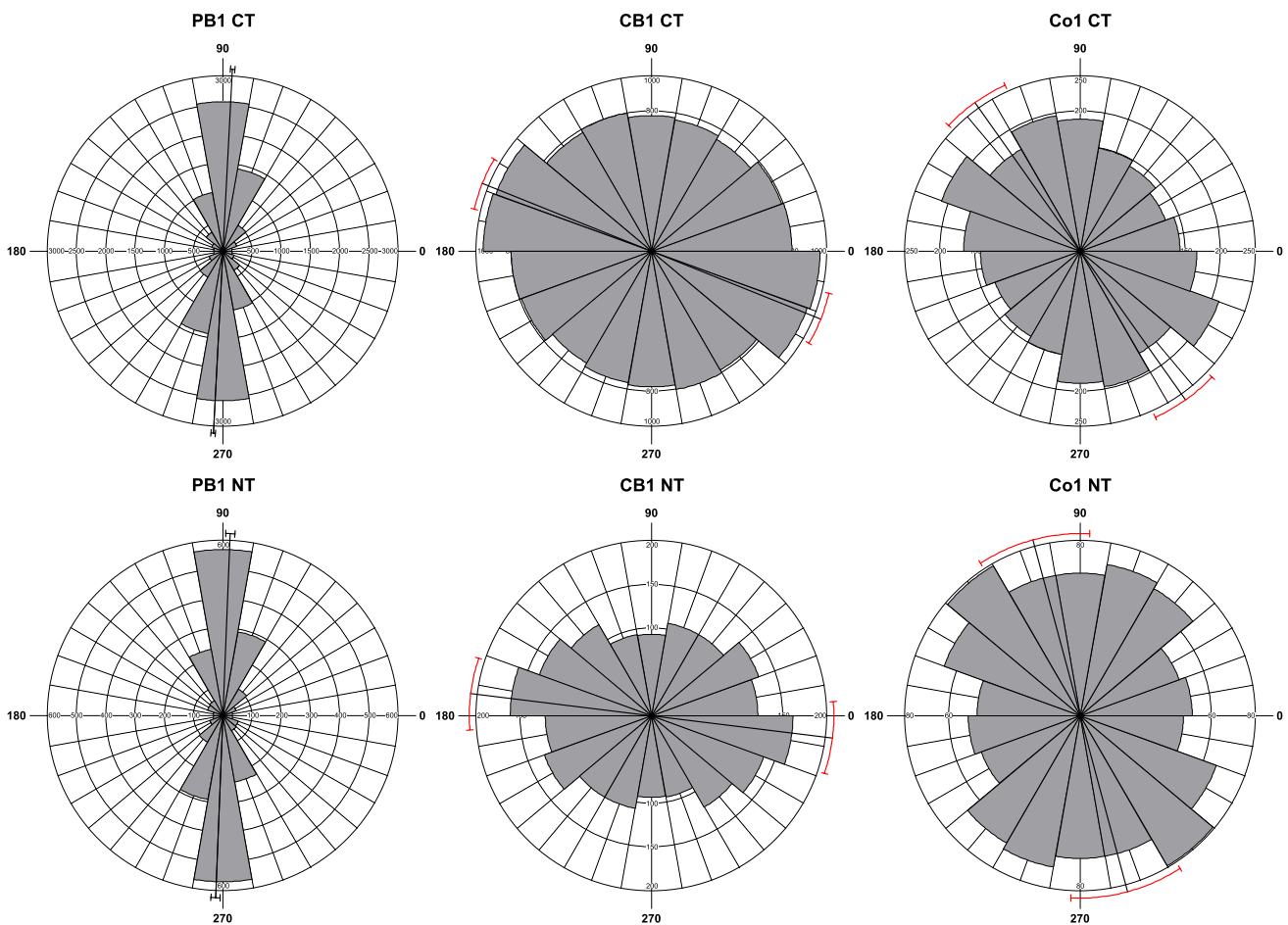


Fig. 20 Rose histograms showing the distribution of azimuth angles in PB1, CB1, and Co1 from filtered μ -CT and NT datasets, with angles treated as axial data (ϕ , angular axis; frequency, radial axis). The mean azimuth angle is shown as a solid line extending across the circumference of the diagram. The arcs to either side of the mean

together indicate the confidence interval of 95% (i.e. $\pm 2 \times SE$). Confidence intervals coloured red indicate that the values may be unreliable owing to the low concentration of the data resulting from near-uniform distributions

Table 3 Statistical results for the polar (θ) and azimuth (ϕ) angles for PB, CB, and Co samples from filtered μ -CT and NT datasets. For the calculation of descriptive statistics, polar angles (0–90°) were treated as linear data, while azimuth angles (0–360°) were treated as axial circular data, with mean values by convention given in the 0–180°

range. For polar angles, a linear standard deviation (SD) is given, while for azimuth angles, the circular standard deviation (CSD) is calculated; consequently, the values are not directly comparable as the permissible ranges are not equal

	θ μ -CT (°)		θ NT (°)		ϕ μ -CT (°)		ϕ NT (°)	
	Mean	SD	Mean	SD	Mean	CSD	Mean	CSD
PB1	37.58	22.72	33.86	22.80	86.94	27.70	87.64	27.53
PB2	28.71	19.84	29.98	20.43	91.74	29.98	90.29	27.80
PB3	25.62	20.89	28.82	23.01	87.65	35.80	88.25	32.68
CB1	17.88	14.31	16.24	14.66	158.17	69.17	172.97	60.69
CB2	18.20	16.25	15.44	14.20	175.94	57.27	169.62	59.85
CB3	16.60	14.25	15.30	15.63	160.92	60.55	121.47	63.98
Co1	16.35	15.60	15.81	15.87	125.31	62.34	105.08	62.46
Co2	16.98	17.43	16.60	16.96	145.83	62.52	143.70	71.06
Co3	20.79	20.33	19.52	19.31	156.92	54.12	158.24	51.13

on the specific manner in which forces are applied, with a larger resultant force on either the interior or exterior margins, the mean ϕ may lie within the smaller or larger of these ranges.

For the PB samples, the objects tend to lie closer to the z -axis than they do for both the CB and Co samples, as indicated by the larger mean value for θ , and the near 90° value for the mean ϕ . This pattern of object orientations also accords to the manner in which forces were applied during primary forming. Unlike for the preparation of coils, during percussion-building, forces were applied primarily in a single direction, namely approximately perpendicular to the walls of the vessel (i.e. in the x -axis). This resulted in forcing the objects towards the z - and y -axes. In previous 2D studies (e.g. Rye 1981), it has been claimed that percussion-building techniques do not display preferential alignment of objects when viewed in the tangential plane and, in general, such a pattern is seen in the PB samples here, as illustrated in Fig. 16 and reflected by the broad shape of the frequency distributions of θ (Fig. 19). However, among the PB samples, a slight tendency towards mean θ values less than 45° indicates a subtle preferential orientation of objects towards the y -axis (Table 3). As described above with regard to projected sizes, the tendency towards mean θ values of slightly less than 45° for the PB samples may be due to the way in which clay was moved during forming to achieve the final shape of the vessels. Consequently, in the case of the PB samples, where for each vessel the value of the radius of the rim is greater than its height, clay was necessarily distributed more in a lateral direction (i.e. in the y -axis) than it was moved vertically (i.e. in the z -axis).

The differences in the mean spherical coordinate angles between forming techniques can also be seen in Fig. 21, where means of θ and ϕ are plotted against each other. The PB samples group around a mean θ of c. 31° and mean ϕ of c. 89° , whereas the CB samples group around a mean θ of c. 17° and mean ϕ of c. 160° . The Co samples can be seen to also cluster close to the CB samples with a mean θ of c. 18° , but, as discussed above, display more variability in the values for mean ϕ . The diagram also shows the generally close agreement between the imaging modalities. The largest discrepancies between μ -CT and NT appear in the values for the mean ϕ , in particular in the absolute values for CB3 (Table 3); however, in relative terms, the differences in CB3 are similar to those for CB1 and CB2.

Robustness analysis of polar and azimuth angles

As with the OI, the strength of using θ and ϕ as means of differentiating forming techniques can be examined further through RA simulations. The results of 5000 simulations for μ -CT and NT, using filtered datasets, are summarised in Table 4. From this, it can be seen that the values of θ and ϕ

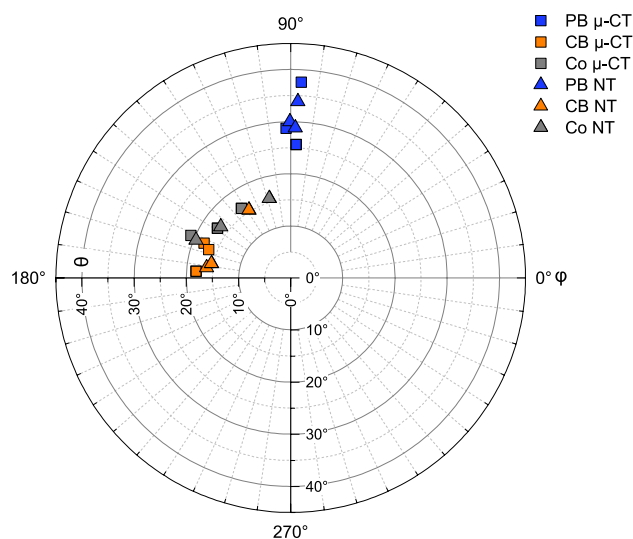


Fig. 21 Polar diagram showing mean polar (θ , radial axis) and azimuth (ϕ , angular axis) angles for objects from coil-built (CB) and percussion-built (PB) vessel samples and coil sections (Co). The CB and Co samples plot close together, while the PB samples also plot close together but at a distance from the CB/Co samples. The results are consistent between μ -CT and NT

from the CB and Co simulations clearly differ from those from the PB simulations. Furthermore, as the confidence intervals do not overlap at mean $\pm 2 \times SD$ (i.e. a 95% probability), it may be said that these differences in mean values are statistically significant. Therefore, as with the OI, the RA simulations confirm that mean polar and azimuth angles are reliable parameters for differentiating between samples made using coil-based techniques and percussion-building.

Conclusions

The results presented here demonstrate that both μ -CT and NT were able to consistently differentiate between the coil-built and TCA percussion-built experimental vessels used in this study through the quantitative evaluation of the 3D orientations of particles and voids (objects) within a fabric tempered with fibrous organic material. In the present study, the patterns of object orientation seen in the percussion- and coil-built vessel samples and the coil sections largely conformed with those previously reported in the literature (e.g. Rye 1981). However, the non-destructive and quantitative attributes of the 3D tomographic imaging methods demonstrated here would appear to offer significant unique advantages over other analytical approaches with regard to the investigation of primary forming techniques.

The non-destructive nature of the techniques has obvious advantages in the study of pottery from archaeological excavations and museum collections, in particular in comparison

Table 4 Statistical results of polar (θ) and azimuth (ϕ) angles for 5000 simulations of PB, CB, and Co filtered datasets for μ -CT and NT. Note that here the SD refers to the spread of the 5000 simulations

	θ μ -CT ($^{\circ}$)			θ NT ($^{\circ}$)			ϕ μ -CT ($^{\circ}$)			ϕ NT ($^{\circ}$)		
	Mean	SD	SE	Mean	SD	SE	Mean	SD	SE	Mean	SD	SE
PB	27.98	1.65	0.02	28.93	1.68	0.02	88.79	1.57	0.02	86.83	3.20	0.05
CB	14.42	1.59	0.02	13.00	1.40	0.02	149.87	29.91	0.42	140.64	26.85	0.38
Co	15.67	1.19	0.02	15.24	1.30	0.02	139.94	5.99	0.09	136.78	10.19	0.14

of mean values, and therefore differs from the SD provided in Table 3 (which refers to the spread in the measurements of the objects within each individual sample)

to the use of tangential thin sections that necessarily result in the destruction of comparatively large samples. Although the samples used in the present study were cut from experimental vessels, tomographic imaging could also be applied to previously broken sherds, or even complete vessels, without necessitating any invasive or destructive sampling. However, to correctly position such sherds within the 3D analytical environment, they would need to display characteristic features (e.g. rim or base) and/or be sufficiently large that their original position within a vessel could be determined. Nonetheless, while tomographic imaging provides detailed information about the structure of fabrics, it gives comparatively little information concerning their composition. In this regard, therefore, conventional thin sections may retain some advantages in that, although destructive, they may provide both structural and compositional information. In practice, therefore, the choice of analytical techniques may depend on the availability and perceived value of the pottery to be studied as well as the range of questions to be addressed.

The quantitative nature of the structural information provided by tomographic imaging also represents a significant development, and offers the opportunity for detailed comparisons between samples, as well as more objective determinations of forming techniques. In the present study, the successful differentiation of vessels made using coil-building and percussion-building forming techniques was derived from both the high degree of spatial information provided for each object, as well as the large number of objects detected within each sample. The ability to describe the orientation of

objects in 3D permits a detailed examination of the ways in which the constituent particles and voids of pottery fabrics respond to forces applied by primary forming techniques. Two methods for describing and quantitatively evaluating the orientation of objects have been proposed here, namely spherical coordinate angles and the Orientation Index (OI) derived from projected sizes. The polar (θ) and azimuth angles (ϕ) together provide detailed descriptions of the full orientations of objects within a 3D space, whereas the OI provides a simple overall measure of the collective orientation of objects, facilitating comparisons between samples. Summaries of the characteristics of percussion- and coil-building forming techniques, as they appear according to these descriptive systems, are given in Table 5, and apply equally to both μ -CT and NT imaging modalities used in the present study.

These quantitative characteristics, as provided by spherical coordinate angles and the OI, can also be described in more general terms. Among the samples analysed in the present study, the objects in the coil-built samples clearly displayed a preferential orientation aligned towards the walls and horizontal rim of each sample. Similarly, preferential orientation was also clearly seen in samples of coil sections, with objects aligned with the length of the coils. Consequently, it appears that much of the orientation of the objects present within the coil sections was retained in the CB samples, but when layers of coils were pressed together during the coil-building process, objects tended to be additionally slightly rotated towards the walls of the

Table 5 Summary of general characteristics of percussion-building and coil-building primary forming techniques, described with regard to distributions of spherical coordinate angles and the OI. (*varying according to the shape and height-to-width ratio of vessel; ** depending on manner of joining of coil layers)

Primary forming technique	Polar angle (θ)	Azimuth angle (ϕ)	Orientation Index (OI)
Percussion-building (PB)	Distribution: positively skewed, broad peak (log-normal) SD: high Mean: c. 30°*	Distribution: symmetric, narrow peak (logistic) CSD: low Mean: c. 90°	c. 0.3
Coil-building (CB)	Distribution: positively skewed, narrow peak (log-normal) SD: low Mean: c. 15°	Distribution: symmetric, broad peak (near uniform) CSD: high Mean: c. 160°/20°**	c. 0.03

vessel. For the percussion-built samples, objects were orientated more closely to the walls of the vessels than in CB samples, but also displayed a slight preferential orientation towards the *y*-axis. From previous studies, it was expected that percussion-built samples would show objects to be randomly distributed within tangential sections (e.g. Rye 1981), and indeed, within the presents study, there was no obvious visually discernible preferential orientation in tangential tomographic slices (Fig. 16, see also Online Resource 1). However, the quantitative analysis demonstrated a slight preferential orientation of objects towards the *y*-axis in all three PB samples. This unexpected result appears to be linked to the comparatively broad shape of the vessels, for which, during forming, clay was moved more towards increasing the diameter of the vessels (i.e. *y*-axis) than it was to increasing their height (*z*-axis), and with objects tending to become aligned towards the direction of the greatest movement. This finding highlights not only the greater sensitivity provided by quantitative analysis over purely visual assessments of individual 2D images, but also the need to consider the influence of vessel shape, as well as forming technique, when interpreting the orientations of objects.

In addition to providing 3D spatial information, tomographic imaging also presented advantages in being able to detect large numbers of objects, which in turn facilitated more robust statistical evaluations. While the number of objects detected varies between fabrics and samples according to the frequencies and types of materials present, tomographic imaging nonetheless benefits from being able to examine the entire volume of a sample as opposed to being limited to only those objects that intersect a given 2D plane (e.g. as seen in a thin section or fresh break surface). Here again, the non-destructive nature of tomographic imaging offers further advantages as, in theory at least, the number of detected objects can be increased by imaging larger portions of samples/vessels without also requiring additional destructive sampling of the artefacts themselves.

However, the number of objects detected is also influenced by the spatial resolutions of tomographic imaging systems. In the present study, the highest (best) spatial resolutions were calculated as c. 100 μm and 300 μm respectively for the $\mu\text{-CT}$ and NT systems used, which are poorer than the highest resolutions typically achievable by other techniques, for instance, digital photomicrographs or scans of thin sections (although in the present study the $\mu\text{-CT}$ system was not run using the instrument's highest resolution). Nonetheless, although these comparatively poor imaging resolutions necessarily resulted in relatively large objects being used for the evaluation of orientations (the median maximum lengths, *L*, of objects with aspect ratio ≤ 0.3 was 1.2 mm and 1.7 mm in $\mu\text{-CT}$ and NT respectively; Fig. 12 and Online Resource 2), sufficient numbers of objects were detected to enable statistically

robust analyses (Table 1). As such, therefore, the comparatively low resolution of tomographic imaging, and that of NT in particular, did not prevent the differentiation of forming techniques among the samples of this study. This finding suggests that while high image resolution may be desirable for some purposes, it is not necessarily a prerequisite for the determination of forming techniques, and, in turn, suggests that conventional CT systems, with resolutions comparable to those of NT, could also be used successfully. The use of imaging systems with more limited resolutions may offer practical advantages not only because they are often more readily available, but also because they are generally designed for the imaging of larger objects than many $\mu\text{-CT}$ systems, and therefore are potentially more suitable for the non-destructive imaging of complete vessels.

While instrument spatial resolution may not be a critical factor with regard to differentiating forming techniques, the shapes of the objects detected are significant. In common with any other analytical approach that attempts to determine forming techniques through the preferential orientation of particles and voids (e.g. using thin sections or fracture surfaces), the 3D object orientation analysis demonstrated in this study necessarily depends on the presence of objects with elongated shapes. The use of dried cattle dung temper in the present study not only resulted in a moderately coarse-textured fabric, but also provided elongated objects that could respond strongly to the forces applied during primary forming. However, it is possible that the dung temper may in fact have had only a comparatively minor influence on the final results. The large majority of the hundreds or thousands of elongated objects selected for analysis for each sample were smaller, often considerably so, than the fibrous particles that typically characterise dried cattle dung (i.e. c. 2 mm, although this too may vary greatly depending on the extent to which particles are broken during the processing of the dung). Similarly, the frequencies of the objects themselves appear too large for them to have all originated from the temper. Consequently, it seems that many of the particles or voids detected in the experimental samples used in this study may have been present within the original clay, and may not necessarily have been derived from the dung temper. While further experimental studies are required, utilising a range of different fabrics and tempers, there are grounds to suspect that quantitative 3D object orientation analysis using tomographic imaging may also be suitable for different types of fabrics, so long as a proportion of the particles and voids present are of elongated shapes.

A further conclusion to be drawn from the present study is the statistically strong nature of the results, as demonstrated by the large differences in the values of the Orientation Index and mean polar and azimuth angles, as well as by the outcomes from the robustness analyses, among the

samples analysed here. This robustness reflects not only the large quantity of data generated by both imaging systems, but also the strength of the fundamental differences in the orientations of the objects imparted by the primary forming techniques when examined in 3D.

As a new imaging technique with regard to the analysis of pottery forming techniques, the present study also investigated whether the known sensitivity of NT to organic materials, especially those naturally containing ^1H , might result in an improved detection of organic inclusions in low-fired ceramics. However, in this regard, the study found that NT did not show any improvements over X-ray-based techniques, with the differences in the number and minimum sizes of objects detected reflecting differences in instrument spatial resolution, rather than differences in the types of materials being detected. This result appears to indicate that, in the samples analysed here, ^1H was lost from the samples during the firing process, or else that it remained only in objects that were too small, or contained too little ^1H , to be detected. Consequently, the results from NT are comparable, notwithstanding differences in resolution, with those from $\mu\text{-CT}$ systems.

While the results of this study are encouraging with regard to the value of tomographic imaging techniques for the non-destructive analysis of primary forming techniques in pottery, it is pertinent nonetheless to note that further developments and applications of the techniques are required. Unlike the comparatively simple fabric and forming techniques used for the experimental samples analysed here, archaeological pottery may be expected to present additional complications, both with regard to a greater variety in the sizes, shapes, and types of inclusions present, but also in the potential diversity of primary forming techniques practiced. Consequently, further work is needed to examine how different materials appear in different tomographic imaging modalities, as well as how they respond to different forming techniques. With regard to the latter, although tomographic imaging additionally has the potential to identify more subtle, and localised, differences in forming techniques (e.g. the specific manner in which coils may have been formed or joined), it may struggle to differentiate between some profoundly different techniques (e.g. slab-building, TCA, pinching, moulding) that display similar patterns of object orientations. Consequently, while the quantitative analysis of the 3D orientations of particles and voids through tomographic imaging represents a powerful analytical tool in the investigation of pottery production strategies and technologies, its greatest value will only be realised when used in combination with other analytical techniques and sources of archaeological information.

Supplementary information The online version contains supplementary material available at <https://doi.org/10.1007/s12520-022-01688-y>.

Acknowledgements The authors express their sincere thanks to Péter Véninger for preparing the experimental samples and for his helpful suggestions. We are very grateful for, and truly appreciate the thorough comments and suggestions of the two anonymous reviewers, who challenged us to greatly improve our manuscript. It was with very great sadness that, during the submission of this article for publication, the authors learnt of the passing of Dr. Roberta Tomber. Her enthusiasm, encouragement, and generosity will always be remembered and appreciated by her colleagues, and the authors acknowledge with particular thanks her insightful thoughts regarding the use of organic tempers.

Author contribution The project was conceived and designed by JG and KB. Data acquisition and processing were led by ZK, IS, VS, and JG, with additional contributions from KB. The manuscript was drafted and edited by JG, ZK, KB, and VS with additional critical contributions from IS. Access to $\mu\text{-CT}$ equipment and supervision was provided by ÁK.

Funding Open access funding provided by Centre for Energy Research. Financial support was provided by the European infrastructure project IPERION CH (654028), and the Hungarian National Research, Development, and Innovation Office through project TKP2021-NVA-19.

Data availability Additional data are provided in the Online Resources.

Declarations

Competing interests The authors declare no competing interests.

Open Access This article is licensed under a Creative Commons Attribution 4.0 International License, which permits use, sharing, adaptation, distribution and reproduction in any medium or format, as long as you give appropriate credit to the original author(s) and the source, provide a link to the Creative Commons licence, and indicate if changes were made. The images or other third party material in this article are included in the article's Creative Commons licence, unless indicated otherwise in a credit line to the material. If material is not included in the article's Creative Commons licence and your intended use is not permitted by statutory regulation or exceeds the permitted use, you will need to obtain permission directly from the copyright holder. To view a copy of this licence, visit <http://creativecommons.org/licenses/by/4.0/>.

References

- Abraham E, Bessou M, Ziégélé A, Hervé M-C, Szentmiklósi L, Kasztovszky Zs, Kis Z, Menu M (2014) Terahertz, X-ray and neutron computed tomography of an Eighteenth Dynasty Egyptian sealed pottery. *Appl Phys A* 117(3):963–972. <https://doi.org/10.1007/s00339-014-8779-3>
- Addinsoft (2021). XLSTAT statistical and data analysis solution. <https://www.xlstat.com>. Accessed 11 Nov 2022
- Banhart J (ed) (2008) Advanced tomographic methods in materials research and engineering. monographs on the physics and chemistry of materials (online edn, Oxford Academic, Oxford. <https://doi.org/10.1093/acprof:oso/9780199213245.001.0001>
- Berg I (2008) Looking through pots: recent advances in ceramics X-radiography. *J Archaeol Sci* 35(5):1177–1188. <https://doi.org/10.1016/j.jas.2007.08.006>
- Berg I (2009) X-radiography of Knossian Bronze Age vessels: assessing our knowledge of primary forming techniques. *The Annual of the British School at Athens* 104:137–173. <https://doi.org/10.1017/S0068245400000228>

- Bernardini F, Leghissa E, Prokop D, Velušček A, De Min A, Drossi D, Donato S, Tuniz C, Princivalle F, Montagnari Kokelj M (2019) X-ray computed microtomography of Late Copper Age decorated bowls with cross-shaped foots from central Slovenia and the Trieste Karst (North-Eastern Italy): technology and paste characterisation. *Archaeol Anthropol Sci* 11(9):4711–4728. <https://doi.org/10.1007/s12520-019-00811-w>
- Bilheux HZ, McGreevy R, Anderson IS (Eds.) (2009) *Neutron imaging and applications*. Springer US. <https://doi.org/10.1007/978-0-387-78693-3>
- Bruker (2005). *SkyScan's NRecon* (1.7.1.6) [Computer software].
- Buzug Th (2008) *Computed tomography*. Springer-Verlag, Berlin Heidelberg. <https://doi.org/10.1007/978-3-540-39408-2>
- Carr C (1990) Advances in ceramic radiography and analysis: applications and potentials. *J Archaeol Sci* 17(1):13–34. [https://doi.org/10.1016/0305-4403\(90\)90013-U](https://doi.org/10.1016/0305-4403(90)90013-U)
- Choleva M, Jung R, Kardamaki E (2020) Working on the potter's wheel: technological insights into Mycenaean pottery production. *Ägypten Und Levante / Egypt and the Levant* 30:219–282
- Coli VL, Gomart L, Pisani DF, Cohen S, Blanc-Féraud L, Leblond J, Binder D (2022) Microcomputed tomography for discriminating between different forming techniques in ancient pottery: new segmentation method and pore distribution recognition. *Archaeometry* 64(1):84–99. <https://doi.org/10.1111/arcm.12693>
- Courty MA, Roux V (1995) Identification of wheel throwing on the basis of ceramic surface features and microfibrils. *J Archaeol Sci* 22(1):17–50. [https://doi.org/10.1016/S0305-4403\(95\)80161-8](https://doi.org/10.1016/S0305-4403(95)80161-8)
- Foster GV (1989) Identification of inclusions in ceramic artifacts by xeroradiography. *J Field Archaeol* 12:373–376
- Fisher NI (1995) *Statistical analysis of circular data*. [Revised paperback edition]. Cambridge University Press, Cambridge
- Fisher NI, Lewis T, Embleton BJJ (1993) *Statistical analysis of spherical data*. [Revised paperback edition]. Cambridge University Press, Cambridge
- Gait JP (2011) *The A-Group/C-Group transition in Lower Nubia (Egypt and Sudan): a review of the pottery evidence* [PhD thesis]. University of Liverpool, Liverpool
- Gosselain OP (2000) Materializing identities: an African perspective. *J Archaeol Method Theory* 7(3):187–217. <https://doi.org/10.1023/A:1026558503986>
- Gosselain, O. P. (2008). Ceramics in Africa. In H. Selin (Ed.), *Encyclopaedia of the history of science, technology, and medicine in non-Western cultures* (pp. 464–476). Springer Netherlands. https://doi.org/10.1007/978-1-4020-4425-0_8911
- Gomart L, Weiner A, Gabriele M, Durrenmath G, Sorin S, Angeli L, Colombo M, Fabbri C, Maggi R, Panelli C, Pisani DF, Radi G, Tozzi C, Binder D (2017) Spiralled patchwork in pottery manufacture and the introduction of farming to Southern Europe. *Antiquity* 91(360):1501–14. <https://doi.org/10.15184/aqy.2017.187>
- Greene AF, Hartley CW, Doumani Dupuy PN, Chinander M (2017) The digital radiography of archaeological pottery: program and protocols for the analysis of production. *J Archaeol Sci* 78:120–133. <https://doi.org/10.1016/j.jas.2016.11.007>
- Hamerow H, Hollevoet Y, Vince A (1994) Migration Period settlements and 'Anglo-Saxon' pottery from Flanders. *Mediev Archaeol* 38(1):1–18. <https://doi.org/10.1080/00766097.1994.11735564>
- Kaestner AP, Kis Z, Radebe MJ, Mannes D, Hovind J, Grünzweig C, Kardjilov N, Lehmann EH (2017) Samples to determine the resolution of neutron radiography and tomography. *Phys Procedia* 88:258–265. <https://doi.org/10.1016/j.phpro.2017.06.036>
- Kahl W-A, Ramming B (2012) Non-destructive fabric analysis of prehistoric pottery using high-resolution X-ray microtomography: a pilot study on the late Mesolithic to Neolithic site Hamburg-Boberg. *J Archaeol Sci* 39(7):2206–2219. <https://doi.org/10.1016/j.jas.2012.02.029>
- Kis Z, Szentmiklósi L, Belgya T, Balaskó M, Horváth LZ, Maróti B (2015) Neutron based imaging and element-mapping at the Budapest Neutron Centre. *Phys Procedia* 69:40–47. <https://doi.org/10.1016/j.phpro.2015.07.005>
- Kovach Computing Services (2013) *Oriana 4.02* [computer software]. Pentraeth, UK. <https://www.kovcomp.co.uk/oriana/index.html>. Accessed 11 Nov 2022
- Kozatsas J, Kotsakis K, Sagris D, David K (2018) Inside out: assessing pottery forming techniques with micro-CT scanning. An example from Middle Neolithic Thessaly. *J Archaeol Sci* 100:102–119. <https://doi.org/10.1016/j.jas.2018.10.007>
- Lehmann EH (2018) Using neutron imaging data for deeper understanding of cultural heritage objects experiences from 15+ years of collaborations. *J Archaeol Sci Rep* 19:397–404. <https://doi.org/10.1016/j.jasrep.2018.02.046>
- Lehmann, E. H., & Kaestner, A. P. (2009). 3D neutron imaging. In R. A. Meyers (Ed.), *Encyclopedia of analytical chemistry* (p. a9123). John Wiley & Sons, Ltd. <https://doi.org/10.1002/9780470027318.a9123>
- Lindahl A, Pikirayi I (2010) Ceramics and change: an overview of pottery production techniques in northern South Africa and eastern Zimbabwe during the first and second millennium AD. *Archaeol Anthropol Sci* 2(3):133–149. <https://doi.org/10.1007/s12520-010-0031-2>
- Livingstone Smith A, Viseyrias A (2010) Shaping Kabambian pottery: identification and definition of technical features. *Open Anthropol J* 3(1):124–141. <https://doi.org/10.2174/1874912701003010124>
- London G (1981) Dung-tempered clay. *J Field Archaeol* 8(2):189–195. <https://doi.org/10.1179/009346981791505049>
- Mannes D, Lehmann EH (2022). Neutron imaging of cultural heritage objects. In S. D'Amico & V. Venuti (Eds.), *Handbook of Cultural Heritage Analysis* (pp. 211–237). Springer International Publishing. https://doi.org/10.1007/978-3-030-60016-7_9
- Middleton A (2005) Ceramics. In J. Lang & A. Middleton (Eds.), *Radiography of Cultural Material* (2nd ed.), 76–95. Butterworth-Heinemann, Oxford
- Neumannová K, Petřík J, Vostrovská I, Dvořák J, Zikmund T, Kaiser J (2017) Variability in coiling technique in LBK pottery inferred by experiments. *Archeologické Rozhledy* 69:172–186
- Nordström H-Å (1972) *Neolithic and A-Group sites* (Vol. 1–2). Läromedelsförlagen, Stockholm
- Park KS, Milke R, Rybacki E, Reinhold S (2019) Application of image analysis for the identification of Prehistoric ceramic production technologies in the North Caucasus (Russia, Bronze/Iron Age). *Heritage* 2:2327–2342. <https://doi.org/10.3390/heritage2030143>
- Pierret A, Moran CJ (1996) Quantification of orientation of pore patterns in X-ray images of deformed clay. *Microsc Microanal Microstruct* 7(5–6):421–431. <https://doi.org/10.1051/mmm:1996141>
- Pierret A, Moran CJ, Bresson L-M (1996) Calibration and visualization of wall-thickness and porosity distributions of ceramics using X-radiography and image processing. *J Archaeol Sci* 23(3):419–428. <https://doi.org/10.1006/jasc.1996.0037>
- Object Research Systems (2022) *Dragonfly 2022.1* [computer software] Object Research Systems (ORS) Inc., Montreal, Canada. <https://theobjects.com/dragonfly/>. Accessed 11 Nov 2022
- Quinn PS (2022) Thin section petrography, geochemistry & scanning electron microscopy of archaeological ceramics. *Archaeopress*, Oxford. <https://doi.org/10.2307/j.ctv2nwg8x4>
- Reedy CL, Anderson J, Reedy TJ (2014a) Quantitative porosity studies of archaeological ceramics by petrographic image analysis. *MRS Online Proc Libr* 1656(1):9–14. <https://doi.org/10.1557/opl.2014.711>
- Reedy CL, Anderson J, Reedy TJ, Liu L (2014b) Image analysis in quantitative particle studies of archaeological ceramic thin

- sections. *Adv Archaeol Pract* 2(4):252–268. <https://doi.org/10.7183/2326-3768.2.4.252>
- Rice PM (2007) *Pottery analysis: a sourcebook* (Second edition) University of Chicago Press, Chicago
- Ross J, Fowler KD, Shai I, Greenfield HJ, Maier AM (2018) A scanning method for the identification of pottery forming techniques at the mesoscopic scale: a pilot study in the manufacture of Early Bronze Age III holemouth jars and platters from Tell es-Safi/Gath. *J Archaeol Sci Rep* 18:551–561. <https://doi.org/10.1016/j.jasrep.2018.01.036>
- Roux V (2019) *Ceramics and society: a technological approach to archaeological assemblages*. Springer Cham. <https://doi.org/10.1007/978-3-030-03973-8>
- Roux V, Courty M-A (1998) Identification of wheel-fashioning methods: technological analysis of 4th–3rd millennium BC Oriental ceramics. *J Archaeol Sci* 25(8):747–763. <https://doi.org/10.1006/jasc.1997.0219>
- Rye OS (1977) Pottery manufacturing techniques: X-ray studies. *Archaeometry* 19(2):205–211. <https://doi.org/10.1111/j.1475-4754.1977.tb00200.x>
- Rye OS (1981). *Pottery technology: principles and reconstruction*. Taraxacum
- Sanger MC (2016) Investigating pottery vessel manufacturing techniques using radiographic imaging and computed tomography: studies from the Late Archaic American Southeast. *J Archaeol Sci Rep* 9:586–598. <https://doi.org/10.1016/j.jasrep.2016.08.005>
- Sanger MC, Thostenson J, Hill M, Cain H (2013) Fibrous twists and turns: early ceramic technology revealed through computed tomography. *Appl Phys A* 111(3):829–839. <https://doi.org/10.1007/s00339-012-7287-6>
- Schindelin J, Arganda-Carreras I, Frise E, Kaynig V, Longair M, Pietzsch T, Preibisch S, Rueden C, Saalfeld S, Schmid B, Tinevez J-Y, White DJ, Hartenstein V, Eliceiri K, Tomancak P, Cardona A (2012) Fiji: an open-source platform for biological-image analysis. *Nat Methods* 9(7):676–682. <https://doi.org/10.1038/nmeth.2019>
- Simulación5 (2022) Simulación 5.0—Free Monte Carlo Excel Add-in & Stochastic Optimization tool. <https://sites.google.com/view/simulacion5/main>. Accessed 11 Nov 2022
- Sterner J, David N (2003) Action on matter: the history of the uniquely African tamper and concave anvil pot-forming technique. *J African Archaeol* 1(1):3–35. <https://doi.org/10.3213/1612-1651-10001>
- Szilágyi V, Kis Z, Szentmiklósi L (2016) Neutron imaging for archaeometry / A neutronos képalkotás archeometriai alkalmazása. *Archeometriai Műhely, XII I(3):157–172*
- Takenouchi K, Yamahana K (2021) Fine pottery shaping techniques in Predynastic Egypt: a pilot study on non-destructive analysis using an X-Ray CT scanning system. *J Archaeol Sci Rep* 37:102989. <https://doi.org/10.1016/j.jasrep.2021.102989>
- Thér R (2016) Identification of pottery-forming techniques using quantitative analysis of the orientation of inclusions and voids in thin sections: identification of pottery-forming techniques. *Archaeometry* 58(2):222–238. <https://doi.org/10.1111/arcm.12166>
- Thér R (2020) Ceramic technology. How to reconstruct and describe pottery-forming practices. *Archaeol Anthropol Sci* 12(8):172. <https://doi.org/10.1007/s12520-020-01131-0>
- Thér R, Květina P, Neumannová K (2019) Coiling or slab building: potential of orientation analysis for identification of forming techniques used by Early Neolithic potters. *J Archaeol Sci Rep* 26:101877. <https://doi.org/10.1016/j.jasrep.2019.101877>
- Thér R, Mangel T (2021) Two trajectories of the development of pottery forming methods in central Europe in the Iron Age: the contribution of analysis of the orientation of components of a ceramic body. *J Archaeol Sci Rep* 35:102717. <https://doi.org/10.1016/j.jasrep.2020.102717>
- Thér R, Toms P (2016) Quantification of the orientation and alignment of aplastic components of a ceramic body as a method for distinguishing among various means of using a rotational device in pottery forming. *J Archaeol Sci Rep* 9:33–43. <https://doi.org/10.1016/j.jasrep.2016.06.048>
- Tomber R, Cartwright C, Gupta S (2011) Rice temper: technological solutions and source identification in the Indian Ocean. *J Archaeol Sci* 38(2):360–366. <https://doi.org/10.1016/j.jas.2010.09.014>
- Türkteki M (2014) Early Bronze Age pottery manufacture in Western Anatolia: identifying hybrid technologies through X-ray analysis. *Anatolica* 40:93–109. <https://doi.org/10.2143/ANA.40.0.3036677>
- Vandiver P (1987) Sequential slab construction; a conservative southwest Asiatic ceramic tradition, ca. 7000–3000 B.C. *Paléorient* 13(2):9–35
- Vlassenbroeck J, Dierick M, Masschaele B, Cnudde V, Van Hoorebeke L, Jacobs P (2007) Software tools for quantification of X-ray microtomography at the UGCT. *Nuclear Instruments and Methods in Physics Research Section A: Accelerators, Spectrometers, Detectors and Associated Equipment* 580(1):442–445. <https://doi.org/10.1016/j.nima.2007.05.073>
- Volume Graphics (2019) VGStudio MAX (3.2.) [Computer software]. Volume Graphics GmbH, Heidelberg, Germany
- Whitbread IK (1996) Detection and interpretation of preferred orientation in ceramic thin sections. In: Higgins T, Main P, Lang J (eds) *Imaging the past: Electronic imaging and computer graphics in museums and archaeology*. The British Museum, pp 173–181
- Williams B (1983) Excavations between Abu Simbel and the Sudan frontier: C-Group, Pan Grave, and Kerma Remains at Adindan cemeteries T, K, U, and J. (Vol. 5). Oriental institute of the University of Chicago, Chicago
- Woods A (1985) An introductory note on the use of tangential thin sections for distinguishing between wheel-thrown and coil/ring built vessels. *Bullet Exp Firing Group* 3:100–114

Publisher's note Springer Nature remains neutral with regard to jurisdictional claims in published maps and institutional affiliations.